

Metric Convolutions: A Unifying Theory to Adaptive Convolutions

Thomas Dagès* Michael Lindenbaum Alfred M. Bruckstein
Technion - Israel Institute of Technology

Abstract

Standard convolutions are prevalent in image processing and deep learning, but their fixed kernel design limits adaptability. Several deformation strategies of the reference kernel grid have been proposed. Yet, they lack a unified theoretical framework. By returning to a metric perspective for images, now seen as two-dimensional manifolds equipped with notions of local and geodesic distances, either symmetric (Riemannian metrics) or not (Finsler metrics), we provide a unifying principle: the kernel positions are samples of unit balls of implicit metrics. With this new perspective, we also propose *metric convolutions*, a novel approach that samples unit balls from explicit signal-dependent metrics, providing interpretable operators with geometric regularisation. This framework, compatible with gradient-based optimisation, can directly replace existing convolutions applied to either input images or deep features of neural networks. Metric convolutions typically require fewer parameters and provide better generalisation. Our approach shows competitive performance in standard denoising and classification tasks.

1 Introduction

In the realm of computer vision and deep learning, traditional convolutions have established themselves as indispensable image processing tools [20, 21], forming the backbone of various neural network architectures, and in particular of the effective convolutional neural networks (CNNs) [28, 45, 49, 22, 35]. Traditional convolutions involve applying fixed-size isotropic $k \times k$ filters to images, a strategy known for its weight-sharing property and parameter efficiency. However, their inherent rigidity becomes evident when dealing with deformable objects, complex spatial transformations, or multi-scale phenomena, limiting their adaptability and, consequently, their effectiveness.

To address this limitation, a diverse research community has explored alternative convolutions. We focus on methods modifying $k \times k$ kernel samples, distinct from those increasing kernel width [18], concatenating [49, 11] or linearly combining [54, 10, 32, 30] responses from different kernels. Dilated convolutions [8, 57, 9, 58] extend the scale of the convolution grid, improving the effective receptive field [37], but rely on a predetermined uniform scale, lacking adaptability to data variations. Spatial transformer networks (STN) [23, 33] employ data-dependent parametrized transformations, such as affine transforms, for feature sampling. Yet, STNs are constrained to predefined transformation families and apply transformations uniformly across the entire feature map. Active convolutions [25] introduce learnable offsets for anisotropic sampling grids but share these offsets across all pixel locations and without data adaptability at inference. Deformable convolutions [15, 59] address these issues by learning signal-dependent offsets at each pixel location. In [56], undesirable offset interactions are recognized, leading to entire deformable convolutions which introduce a single input and location-dependent offset for the entire sampling grid. Another approach, combining dilation and deformable convolution [31], scales the grid to be deformed non-uniformly and signal-dependently. This involves applying multiple deformable convolutions at fixed scales followed by pooling to select the optimal dilation. Unlike other methods discussed here, this approach requires aggregating across multiple deformed convolutions, offering adaptability only within a fixed set of candidate scales. While all these methods have demonstrated improved performance in handling deformations and spatial variations, the theoretical framework underpinning these deformations remains elusive, hindering a comprehensive understanding of their capabilities and limitations.

In response, this paper takes a novel perspective by introducing a unifying framework rooted in metric theory. Metric theory treats images as manifolds endowed with a metric, allowing for

*✉ thomas.dages@cs.technion.ac.il

the computation of distances and neighbourhoods that can deviate from those induced by the typically used Euclidean norm in the image plane. This perspective enables us to reinterpret existing modern convolutions as weighted filtering of samples from the unit ball of a latent metric, effectively linking convolution approaches to implicit metrics. Such an idea echoes yet differs from existing methods working directly on graphs and surfaces [4]. Metric convolutions extend this concept by explicitly incorporating signal and location-dependent parameterised metrics, offering an interpretable, versatile, and adaptable approach to deformable convolutions.

The main contributions of this work are threefold:

- A unifying metric theory that provides geometric interpretability to both existing convolutions and the CNNs employing them.
- Introducing metric convolutions, a novel convolution that can be anisotropic and asymmetric, based on Finsler geometry, that deforms convolution kernels based on explicit, adaptable, and interpretable metrics on the image manifold, promising robustness and versatility.
- The explicit interpretable geometric bias of metric convolutions enable their direct application to full-resolution images outside of neural networks, rather than solely deep inside a CNN. They are also compatible with neural network architectures.

In the following sections, we provide preliminaries on metric geometry (Section 2), present our unifying metric theory to convolutions (Section 3), and explore metric convolutions (Section 4), their theoretical foundations, practical implementation, and empirical evaluations (Section 5).

2 Preliminaries on Metric Geometry

2.1 The concept of distance

In this work, we reinterpret images as parametrised surfaces on the unit plane Ω and explore them from a metric perspective. This perspective had gained popularity prior to the rise of deep learning [42, 43, 34, 7, 12, 48, 47, 5]. Metric geometry focuses on curved spaces, or manifolds, denoted as X , each with well-defined tangent planes $T_x X$ at every point $x \in X$. Manifolds are equipped with metrics, positive functions on the tangent bundle $X \times T_x X \rightarrow \mathbb{R}_+$ guiding local distance calculations. This enables computations of curve lengths, geodesic curves, and geodesic distances between points. Different metrics lead to varying geodesic curves and distances. Henceforth, images are two-dimensional manifolds, also called surfaces, such as grayscale intensity height maps.

Riemann. The common metric choice is the Riemannian metric R , defined by a 2×2 positive definite matrix $M(x)$ at each point x , inducing a scalar product on the tangent plane. Formally, the Riemannian metric is $R_x(u) = \sqrt{u^\top M(x)u}$ at point x and tangent vector $u \in T_x X$. This metric yields symmetric distances, making traversal direction irrelevant. If M is everywhere a scaled identity matrix, then the metric is isotropic, and it is non-uniform yet isotropic if the scale differs between points, although it is sometimes mistakenly called anisotropic [42].

Finsler. While Riemannian metrics create symmetric tangent space neighbourhoods, Finsler metrics provide a generalisation allowing for asymmetric ones. For example, near object boundaries, asymmetric neighbourhoods can prevent neighbours from extending outside the object. Finsler metrics F induce Minkowski norms on tangent spaces, where $F_x(-u)$ and $F_x(u)$ may differ for $u \in T_x X$ at point x . Consequently, local and global distances no longer adhere to symmetry. Formally, a Finsler metric F satisfies $F_x(u) = 0$ if and only if $u = 0$, it obeys the triangular inequality, and is positive-homogeneous, i.e., $F_x(\lambda u) = \lambda F_x(u)$ for any $\lambda > 0$.

Randers. General Finsler metrics are not parametrisable, leading us to consider a subset: Randers metrics. They combine a Riemannian metric, parameterised by M , with a linear drift component, parameterised by $\omega \in T_x X$. Formally, a Randers metric with parameters (M, ω) is defined as $F_x(u) = \sqrt{u^\top M(x)u} + \omega(x)^\top u$. For metric positivity, we require $\|\omega(x)\|_{M^{-1}(x)} < 1$ (details in Proposition A.1). Notably, Riemannian metrics result from $\omega \equiv 0$. Other choices for parametric Finsler metrics are possible, like the (α, β) ones, which induce Kropina or Matsumoto metrics [24].

Henceforth, the metric, most generally Finsler, is written F .

2.2 Unit Balls

In metric geometry, a key concept is the unit ball at point x , a collection of objects within unit distance of x according to the metric F . Depending on the context, the unit ball may refer to different objects.

Unit Tangent Ball. Sometimes, unit balls focus on the tangent plane. The unit tangent ball $B_1^t(x)$ at point x is the set $B_1^t(x) = \{u \in T_x X; F_x(u) \leq 1\}$. For any metric satisfying the triangular inequality, the unit tangent ball (UTB) and its projection onto the image plane are convex sets. In particular, the UTB of a Randers metric is an ellipse, off-centred if $\omega(x) \neq 0$, with equation $u^\top M_x u = (1 - \omega(x)^\top u)^2$. A higher norm of $\omega(x)$ results in less symmetry. In image manifolds, we often project tangent planes onto the image plane and associate the UTB on the tangent space with its projection. If x represents a pixel coordinate, we informally say that $B_1^t(x)$ is the set of pixel coordinates $B_1^t(x) = \{y \in \Omega; F_{X(x)}(y - x) \leq 1\}$.

Unit Geodesic Ball. The unit geodesic ball $B_1^g(x)$ contains all points within a unit geodesic distance from x : $B_1^g(x) = \{y \in X; \text{dist}_F(x, y) \leq 1\}$, where $\text{dist}_F(x, y)$ is the geodesic distance determined by the metric F . It is the minimum length of a smooth curve from x to y (see Appendix A.2). Computing unit geodesic balls (UGB) is challenging as they lack closed-form expressions, unlike UTBs, requiring instead to integrate the metric along geodesics. They can take diverse shapes and may not be convex, especially after projection onto the image plane. As for the UTB, we associate the UGB with its projection on the image plane: $B_1^g(x) = \{y \in \Omega; \text{dist}_F(X(x), X(y)) \leq 1\}$.

3 A Unifying Metric Theory to Convolutions

For simplicity, we assume images are continuous and single-channel, with our theory extendable to multi-channel data. Our domain is $\Omega = [0, 1]^2$, and images are two-dimensional signals $f : \Omega \rightarrow \mathbb{R}$. Discrete images are viewed as samples of the continuous domain, with interpolation (e.g. bilinear) for querying non pixel centre position. Note that presenting image convolutions and their anisotropic variants in the continuum is unusual in the neural network community.

3.1 Preexisting Convolutions

3.1.1 Traditional Fixed Support Convolutions

The convolution $f * g$ of a signal $f : \Omega \rightarrow \mathbb{R}$ with a kernel $g : \Omega \rightarrow \mathbb{R}$ is traditionally¹ defined as

$$(f * g)(x) = \int_{\Omega} f(x + y)g(y)dy. \quad (1)$$

Padding allows to query entries outside Ω . Often, the kernel function g is assumed to be localised on a small compact support $\Delta \subset X$, usually containing 0. The convolution then becomes

$$(f * g)(x) = \int_{\Delta} f(x + y)g(y)dy. \quad (2)$$

Henceforth, we focus on local convolutions. Traditional convolutions assume a fixed kernel support Δ . The weights, i.e., the values of g , are either predefined or learnt. In the discrete world, Δ is usually localised around and includes the entry 0. It is universally discretised into a small $k \times k$ odd square grid, often 3×3 , a prevalent choice in CNNs. We use the word *support* and Δ -based notations for both continuous and sampled discrete convolution supports.

3.1.2 From a Fixed to a Changeable Support

We present three major variations of traditional convolutions based on the shape of the support Δ . While other approaches like [31] may offer different implementation and optimisation strategies, their kernel support formulation typically fits into one of these categories. They originate from prior work in the discrete world. Starting from a $k \times k$ grid forming a reference support Δ^{ref} , each grid cell is shifted to create a new set of k^2 points, forming the modified support Δ . While not traditional convolutions, they maintain the weight sharing principle, with kernel weights $g(y)$ independent of the convolution position x , even if the positions of the support samples y may vary.

¹The convolution notion we use is sometimes called correlation.

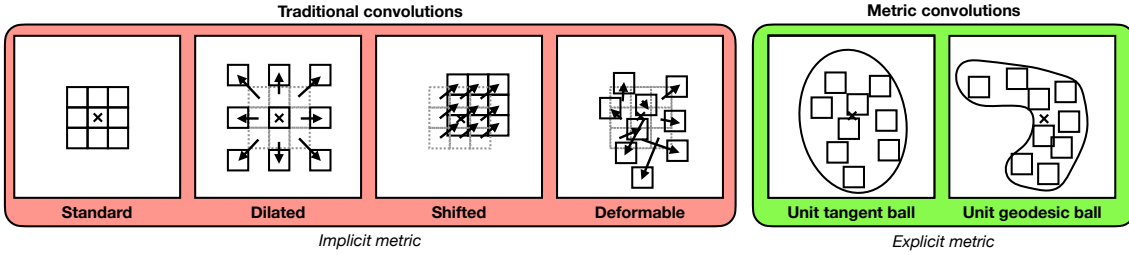


Figure 1: Traditional convolutions, standard or with kernel support deformations, act as weighted averages over unit ball samples of implicit metrics. This theory unifies the various existing convolutions and leads to metric convolutions, a novel convolution paradigm, that samples unit balls of explicit metrics, either learnt or provided by geometric heuristics. The unit balls refer to those in the tangent space or to the geodesic ones on the image manifold, both projected onto the image plane.

Dilated Convolutions. Dilated convolutions, introduced by [8, 9] for neural networks, uniformly scale cell positions in the reference support Δ^{ref} by a dilation factor s^2 , e.g. with $k = 3$ and $s = 4$, the dilated support includes pixels at indices $\{(i, j); i, j \in \{-4, 4, 0\}\}$. Non-standard non-uniform yet isotropic dilated convolution can use different scales s_x per pixel for scale-sensitive filters [31].

Shifted Convolutions. Also called entire deformable convolutions [56], they shift the entire reference kernel support Δ^{ref} by a single offset vector δ_x per pixel x .

Deformable Convolutions. Devised by [15], these convolutions use different offsets δ_x^y for each cell in the reference support Δ^{ref} , inducing complex deformations.

Signal-dependent deformations, as in [15], make deformable convolutions, both entire and regular, and non-standard dilated convolution with adaptive scale [31] non-linear operations. However, computing deformations by traditional convolutions, as in shifted and deformable convolutions, leaves them shift-equivariant. All convolutions presented so far can be seen as specific deformable convolutions with special offset choices. Beyond support deformation, other modifications to the traditional convolution have emerged, such as the modulation idea.

Modulation. Breaking the weight sharing assumption, kernel weights $g(y)$ can be modulated by a number $m_x(y) \in [0, 1]$ depending on x [59, 56].

Generally, non-standard convolution strategies are largely empirical. This diverse field can seem like a multitude of performance-driven tricks lacking a unified theoretical framework. We propose to present and generalise these methods in a systematic way from a metric perspective.

3.2 Unifying Convolutions Through a Metric Lens

All previous convolutions can be expressed as follows.

Theorem 3.1. *If convolution refers to standard, dilated, shifted, or deformable convolutions, then the convolution of a signal f with a kernel g can be expressed as*

$$(f * g)(x) = \int_{\Delta_x} f(x + y)g(y)dm_x(y),$$

where $dm_x(y) = m_x(y)dy$ is a distribution with density $m_x(y) \in [0, 1]$, and Δ_x is a local support depending on x (and sometimes also on f), and it is given by a transformation of a reference local support Δ^{ref} . In the absence of modulation, then $dm_x(y) = dy$.

See Appendix B.1 for a proof. Convolutions discussed so far perform weighted averaging over local neighbourhoods Δ_x , eventually learnt. Modulation introduces non-uniformity in x , and it can be seen from a discrete perspective as a non-uniform sampling probability distribution of Δ_x .

Viewing images as metric manifolds, local neighbourhoods Δ_x can be reinterpreted as the points within a small distance of x for some metric F , taken to be 1 without loss of generality by scaling

²The dilation s represents spacing between kernel elements.

the metric. Thus, we see Δ_x as a unit ball. This suffices to reveal the existence of implicit metrics harnessed by convolutions, according to the following well-known theorem [24].

Theorem 3.2. *A metric is uniquely determined by its unit tangent balls.*

A proof is provided in Appendix B.2 for completeness, and we push to Appendix B.3 a discussion on how to reconstruct the metric from unit geodesic balls. We thus understand the multitude of existing anisotropic convolutions as weighted signal averages in unit balls of implicit, possibly non parametric, metrics F . In this context, modulation acts as a non-uniform distribution for sampling the unit balls.

In practice, we reinterpret discrete convolution kernels Δ_x as finite samples of unit balls. With finite samples, metric uniqueness is lost (see Appendix B.4), yet convolutions described so far (see Figure 1) can be approximately explained using Randers metrics. Other interpretations are possible with different metrics, potentially more suitable as Randers UTBs are confined to ellipses. Standard and dilated convolutions imply an underlying scaled isotropic Riemannian metric. The kernel shift in shifted convolutions can be modelled with the drift component ω of a Randers metric. All three of these can be understood from the perspective of UTBs. Due to constraints on the offset magnitudes, deformable convolution supports usually resemble sampled convex set, which likens to sampling the UTB of a Randers metric. However, UGB sampling is a better interpretation for more involved theoretical deformations resembling the sampling of non-convex sets.

4 Metric Convolutions

With our new metric perspective, existing convolutions are weighted averages over unit balls of an underlying metric, potentially with non-uniform sampling distributions. This understanding allows us to change the convolution paradigm by explicitly constructing a metric F and deriving its unit balls for the filtering operation (see Figure 2). Unit balls should result from a transformation of a reference set, e.g. Δ^{ref} , where weights (output values of g) are well-defined. Termed *metric convolutions*, they generalise existing convolutions relying on implicit metrics by using explicit ones, offering interpretability, strong geometric priors as implicit regularisation, and a fixed small number of parameters for metric encoding, regardless of the number of samples.

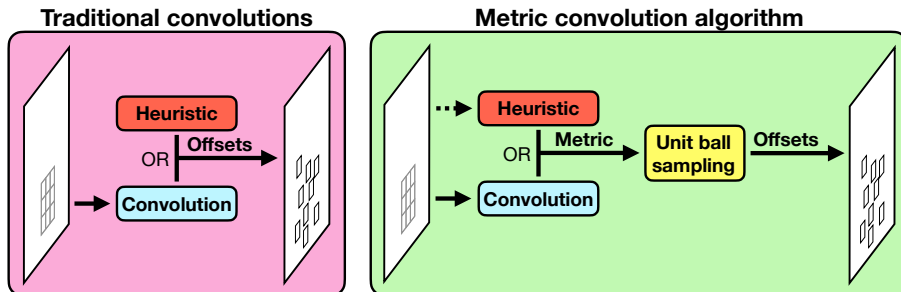


Figure 2: Our metric convolutions compute metrics explicitly for unit ball sampling, while traditional convolutions compute offsets directly. In non-heuristic methods, our intermediate convolution encodes general metrics with only 5 to 7 numbers, compared to $2k^2$ ones for the offsets in a $k \times k$ deformable convolution. Our heuristic methods are compatible with adaptive signal-dependent sampling.

We provide simple, differentiable metric convolution implementations compatible with gradient-based optimisation. We sample unit balls uniformly for simplicity, but can generalise our constructions to modulation by using a parameterised density $m_x(y)$. Our focus is primarily on UTB-based metric convolutions, with an option for UGB-based ones. The general idea for our proposed methods is the following. We consider a class of parametric metrics F^γ , which smoothly depend on location-dependent parameters γ . For instance, we take for Riemannian metrics $\gamma = M$, and for Randers metrics $\gamma = (M, \omega)$. Given γ , we explicitly compute unit balls to define (sampled) neighbourhoods Δ_x for calculating weighted averages. We can choose metric parameters γ based on geometric or image-related properties and can opt for interpretable filtering methods like fixed uniform kernels g . Both kernel weights g and metric parameters γ can be learnt through gradient-based optimisation.

4.1 Unit Tangent Ball Metric Convolution

The unit ball $B_1^t(x)$ is obtained by deforming the unit Euclidean disk. Recall that unit tangent balls (UTB) are convex, e.g. ellipses for Randers metrics. Thus, we can use angles θ as a monotonic parameterisation of the unit circle. Let $y_x(\theta, \gamma) \in B_1^t(x)$ be the point on the unit circle at angle θ for the Finsler metric of parameters γ . That is, $y_x(\theta, \gamma) = \|y_x(\theta, \gamma)\|_2 u_\theta$, where $u_\theta = (\cos \theta, \sin \theta)^\top$. The F_x^γ -unit vector, $y_x(\theta, \gamma)$, satisfies $F_x^\gamma(y_x(\theta, \gamma)) = 1$. The positive homogeneity of the metric implies that $\|y_x(\theta, \gamma)\|_2 = \frac{1}{F_x^\gamma(u_\theta)}$. The unit circle is thus given by the points

$$y_x(\theta, \gamma) = \frac{1}{F_x^\gamma(u_\theta)} u_\theta. \quad (3)$$

With polar coordinates for integration, convolution becomes

$$(f * g)(x) = \int_{s, \theta} f(x + s y_x(\theta, \gamma)) g(s y_x(\theta, \gamma)) ds d\theta. \quad (4)$$

For a signal-dependent metric, we can compute γ directly from the image, e.g. with a standard convolution (by analogy with deformable convolution) we name the *intermediate convolution*. Since M is symmetric definite positive, it requires 3 numbers to be parameterised using its Cholesky decomposition $LL^\top = M$ where L is a lower triangular matrix with positive diagonal. However, we also used a more stable spectral implementation using extra numbers when necessary, where two numbers encode the first eigenfunction of M and the two others are its eigenvalues, eventually adding an additional number encoding the scale of the eigenvalues. As ω requires two numbers, our intermediate convolution only needs 5 to 7 output channels to compute γ , depending on whether we use the Cholesky or spectral implementation, unlike deformable convolution which requires $2k^2$ channels for the offsets if using $k \times k$ samples. In Appendices C.1 and C.2, we explain how to recover $\gamma = (M, \omega)$ from these 5 to 7 numbers while enforcing $\|\omega\|_{M^{-1}(x)} < 1 - \varepsilon_\omega < 1$, where $\varepsilon_\omega \in (0, 1]$ is a hyperparameter controlling the maximum tolerated asymmetry.

By analogy with existing convolutions, we can simply discretise the UTB by sampling k^2 points using polar coordinates $s \in [0, 1]$ and $\theta \in [0, 2\pi]$ (see Appendix C.3), yielding support locations $P_x^\gamma(s, \theta) = s y_x(\theta, \gamma)$ for Δ_x . While straightforward, this implementation is compatible with common neural networks and can be differentiated as explained in Appendix C.4.

4.2 Unit Geodesic Ball Metric Convolution

Efficient geodesic metric convolution implementations are challenging due to costly geodesic extraction (see Appendix C.5). We propose a faster approximation inspired by [13]. It computes geodesic flow fields using normalised gradients of initial Finsler heat flows at pixel x from a simplified local solution with the Finsler Gauss kernel [41, 55]. Then, a set of candidate sample locations initially near x flows along the geodesics for a fixed duration, providing samples of the unit geodesic ball. See Appendix C.6 for full details. Although faster than accurate geodesic extractors [51, 1, 13, 2] and fully differentiable, it is not fast enough for real scenarii such as neural network modules.

5 Experiments

5.1 Denoising Whole Images with a Single Local Convolution

Here, we focus on image denoising, a fundamental task for convolutions as they filter out noise. Surprisingly, modern non-standard convolutions are untested on it, as they are only used in later stages of neural networks for feature learning. In our tests, we add Gaussian noise of standard deviation σ_n to grayscale images. We set the following constraints.

- All methods use $k \times k$ kernel samples with same k .
- All methods apply a single filtering convolution with interpolation allowed for non-pixel centre sampling.
- Convolutions are local. Non-local ones are excluded, e.g. [50, 14, 6].

We explore three filter variations and learning is done either on a single image or on a dataset.

Table 1: Single image denoising results (with noise level $\sigma_n = 0.3$). We also provide the normalised generalisation gap $\delta_{MSE} = \frac{MSE_{test}^{train} - MSE_{train}}{MSE_{train}}$. The parameter ε_ω controls the metric asymmetry.

k	Deformable					Unit tangent ball (ours) [$\varepsilon_\omega = 0.9$]					Unit tangent ball (ours) [$\varepsilon_\omega = 0.1$]				
	5	11	31	51	121	5	11	31	51	121	5	11	31	51	121
MSE	7.26e-3	8.97E-3	1.99E-2	2.83E-2	6.18E-2	8.13E-3	7.43E-3	7.58E-3	8.64E-3	8.28E-3	8.10E-3	7.32E-3	7.45E-3	7.52E-3	7.82E-3
δ_{MSE}	265	74	28	18	6.6	1.1	0.9	1.1	0.8	1.2	1.3	1.1	1.3	1.4	1.5

Geometric heuristic design. To geometrically design filters, we recall that to preserve edges, neighbourhoods should not cross them. Thus, the eigenvectors of M are taken as the image gradient $\nabla f(x)$ and its orthogonal $\nabla f(x)^\top$. Anisotropy is induced by different eigenvalues: a smaller one stretches the unit ball further in its eigendirection due to the inverse in Equation (3). For denoising, a natural choice for the Randers drift component is $\omega \equiv 0$, yet we also test with different asymmetry levels by aligning ω with $\nabla f(x)^\top$ at various scales controlled by a hyperparameter ε_ω . If $\varepsilon_\omega = 1$, then $\omega \equiv 0$. We visualize some unit balls in Figure 3. Notice how UTBs remain convex, while UGBs deform more. Our method gets better filtering (higher PSNR), compared to other manually designed approaches. Further results and implementation details can be found in Appendix D.1.

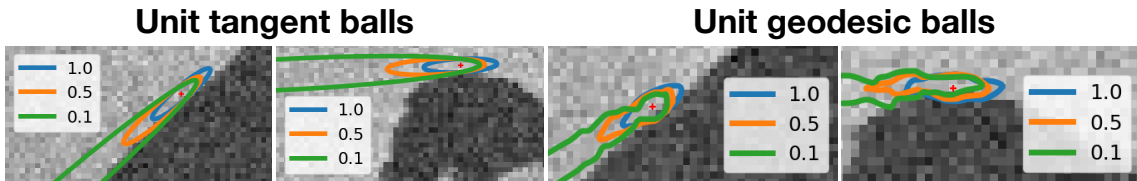


Figure 3: Heuristic unit balls, tangent (left) and geodesic (right). Convolution kernel locations are sampled in them. The different balls correspond to different values of ε_ω controlling the scale of ω .

Learning sample locations only. As an intermediate experiment, between manual design and learning from a training set, we considered learning the metric parameters of UTBs and the offsets of deformable convolutions when applied to a single image. Our method is systematically on par or outperforms deformable convolution (Table 1). As our UTB samples are always derived from a metric, yielding a valuable geometric regularisation, our approach remarkably does not overfit, with low and consistent generalisation errors, in contrast to deformable convolution’s severe overfitting due to the absence of prior knowledge on the structure of the kernel support. For more details and more quantitative and visual results see Appendix D.2.

Learning filtering on a small dataset. In these experiments, we train a single-layer convolution network on standard datasets of 256×256 grayscale images from BSDS300 [38] and PascalVOC Segmentation [19]. Gaussian noise with standard deviation $\sigma_n \in \{0.1, 0.3, 0.5\}$ is added to the images consistently within each experiment. We follow the methodology of [15], making positional parameters, i.e. deformation offsets or metric parameters γ , data-dependent and shift-equivariant by computing them from an intermediate standard $k \times k$ convolution layer (see Figure 2), with the same k as in the final convolution with deformed support. This intermediate layer does multiple convolutions in parallel, i.e. intermediate channels, matching the required number of parameters per pixel. Deformable convolution needs $2k^2$ intermediate channels, while our UTB approach uses only 5 for any k as we use the Cholesky-based implementation. The final convolutions can have fixed uniform kernel weights (FKW) or learnable kernel weights (LKW). We test our method with $\varepsilon_\omega \in \{0.1, 0.9\}$, controlling the metric asymmetry. We provide full training details in Appendix D.3.

Results in Table 2 for learning filtering on datasets show MSE scores and generalisation gaps δ_{MSE} . Our results are on par with deformable convolution, despite our metric UTB convolutions, constrained to ellipses, being theoretically less general. Increasing asymmetry using ε_ω improves performance. Surprisingly, fixing or training kernel weights provides similar results for both methods. Thus, perhaps learning the shape of the kernel is as vital as learning the weights. However, it could also be due to differences in gradient magnitudes for sampling location parameters, as indicated by suggested learning rates (see Appendix D.4).

Table 2: Denoising results on the grayscale versions of BSDS300 and PascalVOC datasets with noise level σ_n . Positional parameters of the $k \times k$ convolutions are learnt with a single regular convolution. The weights of the learnt kernel are either fixed (FKW) or learnt as well (LKW). Top are test MSE losses, bottom are the generalisation gaps δ_{MSE} . Lower is better.

		Deformable						Unit tangent ball (ours)												
		FKW			LKW			$\epsilon_w = 0.1$						$\epsilon_w = 0.9$						
								FKW			LKW			FKW			LKW			
$\sigma_n \backslash k$		5	11	31	5	11	31	5	11	31	5	11	31	5	11	31	5	11	31	
MSE	BSDS300	0.1	1.12e-4	1.83e-4	1.72e-3	1.72e-4	1.70e-4	1.29e-3	1.19e-4	1.19e-4	7.20e-4	1.64e-4	1.32e-4	7.72e-4	1.20e-4	1.24e-4	7.24e-4	1.35e-4	1.32e-4	7.74e-4
		0.3	2.92e-4	2.07e-4	1.89e-3	3.47e-4	3.33e-4	2.10e-3	3.62e-4	3.45e-4	2.04e-3	3.66e-4	3.60e-4	2.09e-3	3.64e-4	3.40e-4	2.05e-3	4.01e-4	3.59e-4	2.11e-3
	0.5	4.91e-4	4.13e-4	3.13e-3	6.44e-4	6.01e-4	3.67e-3	6.67e-4	6.05e-4	3.74e-3	7.15e-4	6.33e-4	3.77e-3	6.96e-4	6.08e-4	3.70e-3	7.03e-4	6.33e-4	3.79e-3	
	PASCALVOC	0.1	8.59e-5	1.56e-4	1.35e-3	1.02e-4	9.81e-5	7.62e-4	1.01e-4	1.00e-4	7.95e-3	1.00e-4	1.12e-4	7.71e-4	1.02e-4	1.02e-4	7.70e-4	1.17e-4	1.12e-4	7.77e-4
		0.3	2.40e-4	2.37e-4	1.84e-3	3.03e-4	2.87e-4	2.14e-3	3.18e-4	2.95e-4	2.27e-3	3.33e-4	2.96e-4	2.05e-3	3.19e-4	2.96e-4	2.28e-3	3.10e-4	2.96e-4	2.06e-3
	0.5	4.28e-4	3.66e-4	3.20e-3	5.77e-4	5.47e-4	4.01e-3	6.05e-4	5.71e-4	4.30e-3	6.23e-4	5.41e-4	3.72e-3	6.37e-4	5.59e-4	4.33e-3	6.20e-4	5.71e-4	3.74e-3	
δ_{MSE}	BSDS300	0.1	0.28	0.14	0.07	0.24	0.20	0.05	0.18	0.21	0.02	0.17	0.21	0.03	0.17	0.21	0.02	0.17	0.21	0.03
		0.3	0.23	0.19	0.001	0.21	0.20	0.05	0.18	0.22	0.04	0.17	0.21	0.04	0.18	0.24	0.04	0.18	0.21	0.04
	0.5	0.22	0.16	0.01	0.20	0.20	0.05	0.19	0.21	0.05	0.19	0.22	0.04	0.18	0.21	0.04	0.19	0.22	0.04	
	PASCALVOC	0.1	0.03	0.01	0.11	0.03	0.03	0.02	0.03	0.03	0.02	0.03	0.03	0.02	0.03	0.03	0.02	0.03	0.03	0.02
		0.3	0.03	0.02	0.01	0.03	0.03	0.01	0.02	0.03	0.01	0.02	0.03	0.02	0.02	0.03	0.01	0.03	0.03	0.03
	0.5	0.01	0.02	0.08	0.02	0.02	0.001	0.02	0.02	0.01	0.02	0.02	0.02	0.02	0.01	0.02	0.01	0.02	0.02	0.02

5.2 From Single to Stacked Convolutions: An Example of CNN Classification

We show how our metric convolutions can be used with neural networks, specifically CNNs. We work on the MNIST [29], Fashion-MNIST [53], CIFAR-10 and CIFAR-100 [27] classification benchmarks. We follow the same methodology as [15, 59, 56] to convert standard convolution modules of a CNN to deformed versions. We try shifted, deformable, and our metric UTB convolutions, to be compared with a baseline using standard convolutions. Specifically, we replace the 3×3 standard convolutions in the later stages, from layer2 to layer4, of a ResNet18 [22] by our metric convolution using the same number of sample locations. As is common given the image resolution, we use a striding of 1 and no pooling in the very first convolution conv1 to avoid losing too much information in the first operation. In our experiments, we either fix the kernel weights (FKW) of non-standard convolutions to uniform values or learn simultaneously sample locations and the weights (LKW). The weights, up to module conversion, are either learned from scratch (SC) or transfer learned (TL) from Imagenet [16] classification with vanilla modules. Due to resource constraints, we only trained a single run on the MNIST and Fashion-MNIST datasets, but train 8 runs on the CIFAR-10 and CIFAR-100 datasets. Full implementation and training details of our and other methods are provided in Appendix D.6.

Table 3: Test accuracies of ResNet18 trained using standard or non-standard convolutions. Higher is better. The main results are those of the LKW-TL columns.

	MNIST				Fashion-MNIST			
	FKW		LKW		FKW		LKW	
	SC	TL	SC	TL	SC	TL	SC	TL
STANDARD	-	-	99.61%	99.66%	-	-	92.37%	93.30%
DEFORMABLE	83.79%	99.16%	99.51%	99.64%	75.50%	90.66%	92.54%	92.74%
SHIFTED	99.11%	99.15%	99.39%	99.64%	82.43%	89.40%	92.75%	93.45%
METRIC UTB (OURS)	99.14%	99.17%	99.64%	99.68%	89.85%	90.87%	92.76%	93.49%

Table 4: Median test accuracies of ResNet18 trained using standard or non-standard convolutions, with 8 independent runs per configuration. Higher is better. In parenthesis is the standard deviation (lower is better). The main results are those of the LKW-TL columns.

	CIFAR-10				CIFAR-100			
	FKW		LKW		FKW		LKW	
	SC	TL	SC	TL	SC	TL	SC	TL
STANDARD	-	-	92.26% ($\pm 0.20\%$)	92.64% ($\pm 0.18\%$)	-	-	70.48% ($\pm 0.29\%$)	70.52% ($\pm 0.38\%$)
TOP1 DEFORMABLE	33.21% ($\pm 2.05\%$)	34.10% ($\pm 6.48\%$)	72.30% ($\pm 7.86\%$)	93.10% ($\pm 0.17\%$)	10.47% ($\pm 0.79\%$)	6.82 ($\pm 1.44\%$)	54.51% ($\pm 8.04\%$)	70.05% ($\pm 0.43\%$)
SHIFTED	37.89% ($\pm 2.06\%$)	29.52% ($\pm 17.19\%$)	86.63% ($\pm 4.49\%$)	92.58% ($\pm 0.28\%$)	14.47% ($\pm 2.40\%$)	2.67 ($\pm 0.66\%$)	47.14% ($\pm 9.05\%$)	68.58% ($\pm 0.48\%$)
METRIC UTB (OURS)	69.83% ($\pm 2.43\%$)	72.15% ($\pm 0.98\%$)	91.83% ($\pm 0.18\%$)	93.07% ($\pm 0.13\%$)	40.63% ($\pm 0.79\%$)	38.04% ($\pm 0.77\%$)	70.03% ($\pm 0.45\%$)	70.38% ($\pm 0.38\%$)
STANDARD	-	-	-	-	-	-	90.30% ($\pm 0.10\%$)	90.03% ($\pm 0.22\%$)
TOP5 DEFORMABLE	-	-	-	-	30.75% ($\pm 1.55\%$)	23.36% ($\pm 3.37\%$)	78.85% ($\pm 5.64\%$)	89.71% ($\pm 0.32\%$)
SHIFTED	-	-	-	-	37.73% ($\pm 3.72\%$)	10.67% ($\pm 2.21\%$)	74.34% ($\pm 6.56\%$)	88.77% ($\pm 0.29\%$)
METRIC UTB (OURS)	-	-	-	-	71.70% ($\pm 0.78\%$)	69.22% ($\pm 0.63\%$)	90.42% ($\pm 0.19\%$)	90.23% ($\pm 0.17\%$)

We provide test accuracies in Tables 3 and 4 and list the following observations. 1) Our metric CNN systematically outperforms both deformable and shifted convolutions, with only rare occasions where it is only on par with deformable convolution. 2) Our geometric construction is a powerful prior leading to a strong implicit bias since 2)a) like standard CNNs, our metric CNN is barely affected by training from scratch (SC), sometimes even improving the result, and 2)b) our metric CNNs still perform reasonably well when the weights of the convolution kernels are fixed (FKW).

In comparison, CNNs using either deformable or shifted convolutions see a significant performance drop when trained from scratch, especially on CIFAR-10 and CIFAR-100, and act close to random predictors when the convolution kernels are fixed. While it could be argued that shifted convolutions has a stronger prior, since its kernel position has only 2 degrees of freedom compared to the 5 to 7 ones for our metric kernel, these results prove that a geometric approach backed by a metric theory has better regularisation than an efficient yet solely empirical approach. 3) The results of our metric CNNs have a significantly lower standard deviation, even in the rare case when their results are only on par with those of deformable convolution. As such, our CNNs are more stable, and we can rely on them more should we only be able to afford a single training run.

We also plot GradCAM [44] visualisations on random images of randomly selected classes from the CIFAR-100 test set (for LKW-TL trained networks) in Figure 4. These heatmaps are computed as the ReLU of the linear combination of the feature representations after the last convolution layer, where the weights of the combination are given by the gradient with respect to the groundtruth label. They are then resized to the original image resolution and superimposed on the image. GradCAMs visually indicate what locations in the image positively contribute to the prediction of the correct class. We see that our metric CNN better focuses than CNNs using other types of convolutions on the relevant objects and their meaningful parts, e.g. the face or fins of a dolphin, rather than on the background. It is also able to handle multiple instances unlike the other CNNs, rather than focusing on one of them. These visual results point towards the superiority of CNNs with metric convolutions rather than other existing types of convolutions. Not only are metric convolutions more interpretable due to the use of metric theory, but the results seem more interpretable as well. Our experiments demonstrate how to combine metric convolutions with complex neural architectures for high level tasks and that networks benefit from our metric approach to convolutions.

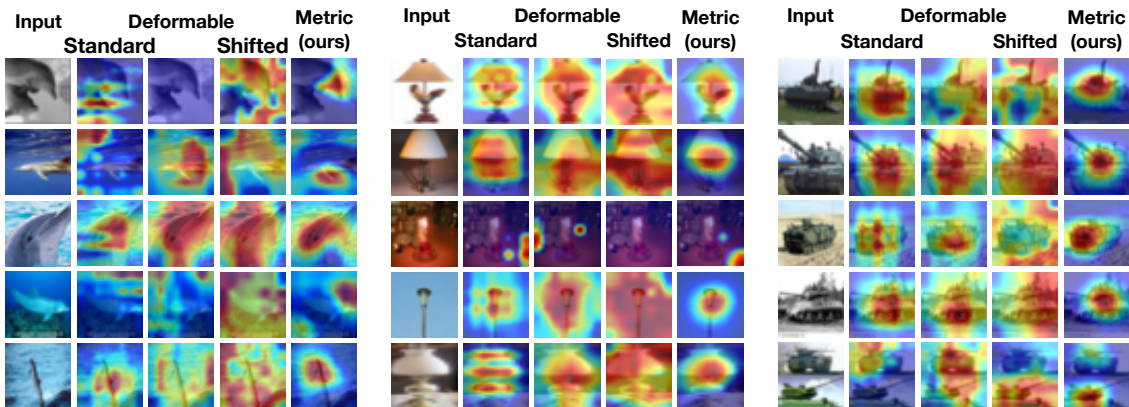


Figure 4: GradCAM visualisations on random samples of the *dolphin*, *lamp*, and *tank* classes of CIFAR-100. Our metric CNN better focuses on the relevant objects and its meaningful parts and is able to handle multiple instances unlike the other CNNs. Red means high values, blue means 0.

6 Conclusion

By viewing images as metric manifolds, we provided a unified theory explaining the various existing deformed convolution operators as methods sampling unit balls of various implicit metrics. With this new perspective, we designed a novel framework for adaptive image convolutions, called metric convolutions, that sample unit balls of explicit metrics of various complexity to compute kernel locations. We demonstrated the advantages of our method, providing competitive results on standard benchmarks, while improving interpretability and carrying strong geometric regularisation. We hope that this work will help popularise the image manifold paradigm and the use of Finsler metrics to the modern computer vision and deep learning community.

Limitations and future works. First, our choice of Randers metrics constrains the unit tangent balls to ellipses. Other convex shapes would be of interest, yielding different types of Finsler unit balls. Second, our implementation of unit geodesic ball metric convolutions is currently too slow for practical use. Improving it and using them in neural networks is a future research direction. Third, our metric convolutions inherit the drawback shared by all non-standard convolutions, which is

the need to store in memory sampling offset locations per pixel. This high memory footprint can make learning on high resolution images challenging especially when working on high batch sizes. Consequentially, we focused on smaller resolution benchmarks, and leave tests on higher resolution data to future works. We also focused on a couple of tasks, yet we are intrigued by how beneficial our metric-based learned representations would be for downstream tasks. Viewing individual images as a metric manifold is largely uncharted in modern machine learning and requires further study.

References

- [1] F. Benmansour, G. Carlier, G. Peyré, and F. Santambrogio. Derivatives with respect to metrics and applications: subgradient marching algorithm. *Numerische Mathematik*, 116:357–381, 2010.
- [2] T. Bertrand, N. Makaroff, and L. D. Cohen. Fast marching energy CNN. In *International Conference on Scale Space and Variational Methods in Computer Vision*, pages 276–287. Springer, 2023.
- [3] J. F. Bonnans, G. Bonnet, and J.-M. Mirebeau. A linear finite-difference scheme for approximating Randers distances on cartesian grids. *ESAIM: Control, Optimisation and Calculus of Variations*, 28:45, 2022.
- [4] D. Boscaini, J. Masci, E. Rodolà, and M. Bronstein. Learning shape correspondence with anisotropic convolutional neural networks. *Advances in neural information processing systems*, 29, 2016.
- [5] A. Buades, B. Coll, and J.-M. Morel. A review of image denoising algorithms, with a new one. *Multiscale modeling & simulation*, 4(2):490–530, 2005.
- [6] A. Buades, B. Coll, and J.-M. Morel. Non-local means denoising. *Image Processing On Line*, 1:208–212, 2011.
- [7] V. Caselles, R. Kimmel, and G. Sapiro. Geodesic active contours. In *Proceedings of IEEE international conference on computer vision*, pages 694–699. IEEE, 1995.
- [8] L.-C. Chen, G. Papandreou, I. Kokkinos, K. Murphy, and A. L. Yuille. Semantic image segmentation with deep convolutional nets and fully connected CRFs. *3rd International Conference on Learning Representations*, 2015.
- [9] L.-C. Chen, G. Papandreou, I. Kokkinos, K. Murphy, and A. L. Yuille. Deeplab: Semantic image segmentation with deep convolutional nets, atrous convolution, and fully connected CRFS. *IEEE transactions on pattern analysis and machine intelligence*, 40(4):834–848, 2017.
- [10] Y. Chen, X. Dai, M. Liu, D. Chen, L. Yuan, and Z. Liu. Dynamic convolution: Attention over convolution kernels. In *Proceedings of the IEEE/CVF conference on computer vision and pattern recognition*, pages 11030–11039, 2020.
- [11] F. Chollet. Xception: Deep learning with depthwise separable convolutions. In *Proceedings of the IEEE conference on computer vision and pattern recognition*, pages 1251–1258, 2017.
- [12] L. D. Cohen and R. Kimmel. Global minimum for active contour models: A minimal path approach. *International journal of computer vision*, 24:57–78, 1997.
- [13] K. Crane, C. Weischedel, and M. Wardetzky. Geodesics in heat: A new approach to computing distance based on heat flow. *ACM Transactions on Graphics (TOG)*, 32(5):1–11, 2013.
- [14] K. Dabov, A. Foi, V. Katkovnik, and K. Egiazarian. Image denoising by sparse 3-d transform-domain collaborative filtering. *IEEE Transactions on image processing*, 16(8):2080–2095, 2007.
- [15] J. Dai, H. Qi, Y. Xiong, Y. Li, G. Zhang, H. Hu, and Y. Wei. Deformable convolutional networks. In *Proceedings of the IEEE international conference on computer vision*, pages 764–773, 2017.
- [16] J. Deng, W. Dong, R. Socher, L.-J. Li, K. Li, and L. Fei-Fei. Imagenet: A large-scale hierarchical image database. In *2009 IEEE conference on computer vision and pattern recognition*, pages 248–255. Ieee, 2009.

- [17] M. Desbrun, M. Meyer, P. Schröder, and A. H. Barr. Implicit fairing of irregular meshes using diffusion and curvature flow. In *Proceedings of the 26th Annual Conference on Computer Graphics and Interactive Techniques, SIGGRAPH '99*, page 317–324, USA, 1999.
- [18] X. Ding, X. Zhang, J. Han, and G. Ding. Scaling up your kernels to 31x31: revisiting large kernel design in CNNs. In *Proceedings of the IEEE/CVF conference on computer vision and pattern recognition*, pages 11963–11975, 2022.
- [19] M. Everingham, L. Van Gool, C. K. Williams, J. Winn, and A. Zisserman. The Pascal visual object classes (VOC) challenge. *International journal of computer vision*, 88:303–338, 2010.
- [20] D. A. Forsyth and J. Ponce. *Computer vision: A modern approach*. prentice hall professional technical reference, 2002.
- [21] I. Goodfellow, Y. Bengio, and A. Courville. *Deep learning*. MIT press, 2016.
- [22] K. He, X. Zhang, S. Ren, and J. Sun. Deep residual learning for image recognition. In *Proceedings of the IEEE conference on computer vision and pattern recognition*, pages 770–778, 2016.
- [23] M. Jaderberg, K. Simonyan, A. Zisserman, et al. Spatial transformer networks. *Advances in neural information processing systems*, 28, 2015.
- [24] M. A. Javaloyes and M. Sánchez. On the definition and examples of Finsler metrics. *arXiv preprint arXiv:1111.5066*, 2011.
- [25] Y. Jeon and J. Kim. Active convolution: Learning the shape of convolution for image classification. In *Proceedings of the IEEE conference on computer vision and pattern recognition*, pages 4201–4209, 2017.
- [26] D. P. Kingma and J. Ba. Adam: A method for stochastic optimization. *arXiv preprint arXiv:1412.6980*, 2014.
- [27] A. Krizhevsky. Learning multiple layers of features from tiny images. 2009.
- [28] A. Krizhevsky, I. Sutskever, and G. E. Hinton. Imagenet classification with deep convolutional neural networks. *Advances in neural information processing systems*, 25, 2012.
- [29] Y. LeCun, L. Bottou, Y. Bengio, and P. Haffner. Gradient-based learning applied to document recognition. *Proceedings of the IEEE*, 86(11):2278–2324, 1998.
- [30] C. Li, A. Zhou, and A. Yao. Omni-dimensional dynamic convolution. *arXiv preprint arXiv:2209.07947*, 2022.
- [31] W. Li, B. Li, C. Yuan, Y. Li, H. Wu, W. Hu, and F. Wang. Anisotropic convolution for image classification. *IEEE Transactions on Image Processing*, 29:5584–5595, 2020.
- [32] Y. Li, Y. Chen, X. Dai, M. Liu, D. Chen, Y. Yu, L. Yuan, Z. Liu, M. Chen, and N. Vasconcelos. Revisiting dynamic convolution via matrix decomposition. *arXiv preprint arXiv:2103.08756*, 2021.
- [33] C.-H. Lin and S. Lucey. Inverse compositional spatial transformer networks. In *Proceedings of the IEEE Conference on Computer Vision and Pattern Recognition*, pages 2568–2576, 2017.
- [34] M. Lindenbaum, M. Fischer, and A. Bruckstein. On Gabor’s contribution to image enhancement. *Pattern recognition*, 27(1):1–8, 1994.
- [35] Z. Liu, H. Mao, C.-Y. Wu, C. Feichtenhofer, T. Darrell, and S. Xie. A convnet for the 2020s. In *Proceedings of the IEEE/CVF conference on computer vision and pattern recognition*, pages 11976–11986, 2022.
- [36] I. Loshchilov and F. Hutter. SGDR: Stochastic gradient descent with warm restarts. *arXiv preprint arXiv:1608.03983*, 2016.
- [37] W. Luo, Y. Li, R. Urtasun, and R. Zemel. Understanding the effective receptive field in deep convolutional neural networks. *Advances in neural information processing systems*, 29, 2016.

- [38] D. Martin, C. Fowlkes, D. Tal, and J. Malik. A database of human segmented natural images and its application to evaluating segmentation algorithms and measuring ecological statistics. In *Proceedings Eighth IEEE International Conference on Computer Vision. ICCV 2001*, volume 2, pages 416–423. IEEE, 2001.
- [39] M. Meyer, M. Desbrun, P. Schröder, and A. H. Barr. Discrete differential-geometry operators for triangulated 2-manifolds. In *Visualization and mathematics III*, pages 35–57. Springer, 2003.
- [40] J.-M. Mirebeau. Efficient fast marching with Finsler metrics. *Numerische mathematik*, 126(3):515–557, 2014.
- [41] S.-i. Ohta and K.-T. Sturm. Heat flow on Finsler manifolds. *Communications on Pure and Applied Mathematics: A Journal Issued by the Courant Institute of Mathematical Sciences*, 62(10):1386–1433, 2009.
- [42] P. Perona and J. Malik. Scale-space and edge detection using anisotropic diffusion. *IEEE Transactions on pattern analysis and machine intelligence*, 12(7):629–639, 1990.
- [43] L. I. Rudin, S. Osher, and E. Fatemi. Nonlinear total variation based noise removal algorithms. *Physica D: nonlinear phenomena*, 60(1-4):259–268, 1992.
- [44] R. R. Selvaraju, M. Cogswell, A. Das, R. Vedantam, D. Parikh, and D. Batra. Grad-cam: Visual explanations from deep networks via gradient-based localization. In *Proceedings of the IEEE international conference on computer vision*, pages 618–626, 2017.
- [45] K. Simonyan and A. Zisserman. Very deep convolutional networks for large-scale image recognition. *arXiv preprint arXiv:1409.1556*, 2014.
- [46] L. N. Smith. Cyclical learning rates for training neural networks. In *2017 IEEE winter conference on applications of computer vision (WACV)*, pages 464–472. IEEE, 2017.
- [47] N. Sochen, R. Kimmel, and A. M. Bruckstein. Diffusions and confusions in signal and image processing. *Journal of Mathematical Imaging and Vision*, 14:195–209, 2001.
- [48] N. Sochen, R. Kimmel, and R. Malladi. A general framework for low level vision. *IEEE transactions on image processing*, 7(3):310–318, 1998.
- [49] C. Szegedy, W. Liu, Y. Jia, P. Sermanet, S. Reed, D. Anguelov, D. Erhan, V. Vanhoucke, and A. Rabinovich. Going deeper with convolutions. In *Proceedings of the IEEE conference on computer vision and pattern recognition*, pages 1–9, 2015.
- [50] C. Tomasi and R. Manduchi. Bilateral filtering for gray and color images. In *Sixth international conference on computer vision (IEEE Cat. No. 98CH36271)*, pages 839–846. IEEE, 1998.
- [51] S. R. S. Varadhan. On the behavior of the fundamental solution of the heat equation with variable coefficients. *Communications on Pure and Applied Mathematics*, 20(2):431–455, 1967.
- [52] S. Weber, T. Dagès, M. Gao, and D. Cremers. Finsler-Laplace-Beltrami operators with application to shape analysis. *arXiv preprint arXiv:2404.03999*, 2024.
- [53] H. Xiao, K. Rasul, and R. Vollgraf. Fashion-MNIST: A novel image dataset for benchmarking machine learning algorithms. *arXiv preprint arXiv:1708.07747*, 2017.
- [54] B. Yang, G. Bender, Q. V. Le, and J. Ngiam. Condconv: Conditionally parameterized convolutions for efficient inference. *Advances in neural information processing systems*, 32, 2019.
- [55] F. Yang, L. Chai, D. Chen, and L. D. Cohen. Geodesic via asymmetric heat diffusion based on Finsler metric. In *Asian Conference on Computer Vision (ACCV)*, Springer, pages 371–386, 2018.
- [56] B. Yu, L. Jiao, X. Liu, L. Li, F. Liu, S. Yang, and X. Tang. Entire deformable convnets for semantic segmentation. *Knowledge-Based Systems*, 250:108871, 2022.
- [57] F. Yu and V. Koltun. Multi-scale context aggregation by dilated convolutions. *arXiv preprint arXiv:1511.07122*, 2015.

- [58] F. Yu, V. Koltun, and T. Funkhouser. Dilated residual networks. In *Proceedings of the IEEE conference on computer vision and pattern recognition*, pages 472–480, 2017.
- [59] X. Zhu, H. Hu, S. Lin, and J. Dai. Deformable convnets v2: More deformable, better results. In *Proceedings of the IEEE/CVF conference on computer vision and pattern recognition*, pages 9308–9316, 2019.

A Finsler and Randers Metrics: Further Details

We refer the interested reader for more information on Finsler and Randers metrics to the specialised Finsler literature, such as [41, 40, 3]. The details mentioned in this section are well-known in the community, but we put them here so that our paper is self-contained.

A.1 Randers Metric Positivity

The positivity of the Randers metric F is ensured by $\|\omega\|_{M^{-1}} < 1$. In fact, we can generalise the statement in the following proposition that links the Randers metric with the regular L_2 norm.

Proposition A.1. *Let $0 < \varepsilon < 1$. If for any point x on the manifold we have $\|\omega(x)\|_{M^{-1}(x)} \leq 1 - \varepsilon$, then the metric satisfies $F_x(u) \geq \varepsilon\|u\|_2$ for any $u \in T_xX$. In particular, if $\|\omega\|_{M^{-1}(x)} < 1$, then $F_x(u) > 0$ for any $u \neq 0$.*

Proof. All tangent vectors of T_xX can be rewritten as $M(x)^{-1}u$. We then have

$$F_x(M(x)^{-1}u) = \sqrt{u^\top M(x)^{-1}u + \omega(x)^\top M(x)^{-1}u} \quad (5)$$

$$= \|M(x)^{-\frac{1}{2}}u\|_2 + \langle M(x)^{-\frac{1}{2}}\omega(x), M(x)^{-\frac{1}{2}}u \rangle. \quad (6)$$

The Cauchy-Schwartz inequality provides that

$$|\omega(x)^\top M(x)^{-1}u| \leq \|M(x)^{-\frac{1}{2}}\omega(x)\|_2 \|M(x)^{-\frac{1}{2}}u\|_2. \quad (7)$$

The assumption on ω can be rewritten as

$$\|M(x)^{-\frac{1}{2}}\omega(x)\| \leq 1 - \varepsilon. \quad (8)$$

Thus, for any tangent vector u , we get $F_x(M(x)^{-1}u) \geq \varepsilon\|M(x)^{-1}u\|_2$, and so for any such u , we obtain the desired result $F_x(u) \geq \varepsilon\|u\|_2$. \square

A.2 Finsler Geodesic Distances

Given a Finsler metric F , the geodesic distance $\text{dist}_F(x, y)$ between points x and y on the manifold is given by the minimum length of a smooth curve $c(t)$ from x to y

$$\text{dist}_F(x, y) = \min_{\substack{c(t) \\ c(0)=x \text{ and } c(1)=y}} \int_{[0,1]} F_{c(t)}\left(\frac{\partial c}{\partial t}(t)\right) dt. \quad (9)$$

In particular, the orientation x to y is important for non Riemannian asymmetric metrics, as then $F_{c(t)}\left(\frac{\partial c}{\partial t}(t)\right)$ may differ from $F_{c(t)}\left(-\frac{\partial c}{\partial t}(t)\right)$.

A.3 Dual Randers Metric

The dual metric of a Finsler metric plays a key role in differential geometry on manifolds as it systematically appears in major differential equations, such as the Eikonal equation or the heat diffusion equation. Formally the dual metric of F is the metric F^* such that

$$F_x^*(u) = \max\{u^\top v; v \in T_xX, F_x(v) \leq 1\}. \quad (10)$$

One can easily verify that it satisfies the Finsler metric axioms. If F is a Randers metric parameterised by (M, ω) , then the dual metric F^* is also a Randers metric. It is parameterised by (M^*, ω^*) , which are explicitly given by (M, ω) .

Proposition A.2. *The dual of a Randers metric F parameterised by (M, ω) is a Randers metric F^* . If we denote $\alpha = 1 - \|\omega\|_{M^{-1}}^2 > 0$, then the parameters (M^*, ω^*) of F^* are given by*

$$\begin{cases} M^* = \frac{1}{\alpha^2} \left(\alpha M^{-1} + (M^{-1}\omega)(M^{-1}\omega)^\top \right), \\ \omega^* = -\frac{1}{\alpha} M^{-1}\omega. \end{cases}$$

Proof. To ease notations, we drop the explicit dependence on x . Although the definition of the dual Randers metric is given in Equation (10), since F is positive homogeneous it is also given by

$$F^*(u) = \max \left\{ \frac{u^\top v}{F(v)}; v \neq 0 \right\}. \quad (11)$$

Therefore, the inverse solves the minimisation problem $\frac{1}{F^*(u)} = \min \left\{ \frac{F(v)}{u^\top v}; v \neq 0 \right\}$. Likewise, by positive homogeneity, we have that the inverse of the dual metric satisfies the constrained minimisation problem

$$\frac{1}{F^*(u)} = \min \{ F(v); u^\top v = 1 \}. \quad (12)$$

We can also solve this constrained optimisation problem with Lagrangian optimisation. The Lagrangian is given by $L(v, \lambda) = F(v) + \lambda u^\top v$. To satisfy the KKT conditions, we differentiate L with respect to v and set the gradient to 0. The optimal v^* thus satisfies

$$M \frac{v^*}{\|v^*\|_M} + \omega + \lambda u = 0. \quad (13)$$

By computing the scalar product of this equation with v^* , and recalling that the constraint guarantees $u^\top v^* = 1$, we get, since $F(v^*) = \sqrt{v^{*\top} M v^*} + v^{*\top} \omega$, that $\lambda = -F(v^*)$. Recall that v^* solves the minimisation problem Equation (12). Therefore,

$$\lambda = -\frac{1}{F^*(v)}. \quad (14)$$

Returning to Equation (13), we can compute $\|\omega + \lambda u\|_{M^{-1}}$ as

$$\|\omega + \lambda u\|_{M^{-1}} = \frac{\|M v^*\|_{M^{-1}}}{\|v^*\|_M} = 1. \quad (15)$$

By squaring this equation, we obtain a polynomial of degree two for which λ is a root

$$\lambda^2 \|u\|_{M^{-1}}^2 + 2\lambda \langle \omega, u \rangle_{M^{-1}} + \|\omega\|_{M^{-1}}^2 - 1 = 0. \quad (16)$$

Let $\alpha = 1 - \|\omega\|_{M^{-1}}^2 > 0$. The roots are then given by

$$\lambda_{\pm} = \frac{-\langle \omega, u \rangle_{M^{-1}} \pm \sqrt{\langle \omega, u \rangle_{M^{-1}}^2 + \|u\|_{M^{-1}}^2 \alpha}}{\|u\|_{M^{-1}}^2}. \quad (17)$$

Clearly, we have $\lambda_- < 0 < \lambda_+$ for $u \neq 0$. However, $\lambda < 0$ as $\lambda = -F(v^*)$ and the metric is always positive. As such, $\lambda = \lambda_-$. Inverting Equation (14), we get

$$\begin{aligned} F^*(u) &= \frac{\|u\|_{M^{-1}}^2}{\langle \omega, u \rangle_{M^{-1}} + \sqrt{\langle \omega, u \rangle_{M^{-1}}^2 + \|u\|_{M^{-1}}^2 \alpha}} \\ &= \sqrt{u^\top \frac{1}{\alpha^2} (\alpha M^{-1} + M^{-1} \omega \omega^\top M^{-1}) u} \\ &\quad - \frac{1}{\alpha} \langle \omega, u \rangle_{M^{-1}}, \end{aligned} \quad (18)$$

$$\quad (19)$$

where the classical trick $\frac{1}{x+\sqrt{y}} = \frac{x-\sqrt{y}}{x^2-y}$ was used to remove the square root from the denominator. We now identify the dual metric F^* as a Randers metric associated to (M^*, ω^*) as initially claimed

$$\begin{cases} M^* = \frac{1}{\alpha^2} (\alpha M^{-1} + (M^{-1} \omega)(M^{-1} \omega)^\top), \\ \omega^* = -\frac{1}{\alpha} M^{-1} \omega. \end{cases} \quad (20)$$

□

When studying the propagation of a wave front [40], the dual metric naturally appears yielding the Finsler Eikonal equation

$$F_x^*(-\nabla f) = 1. \quad (21)$$

Likewise, by observing that the heat equation in the Riemannian case is given by the gradient flow of the Dirichlet energy, we can descend on the dual energy $\frac{1}{2}F_x^*(u)^2$ to define the Finsler heat equation [41, 3]

$$\frac{\partial f}{\partial t} = \text{div}(F_x^*(\nabla f)\nabla F_x^*(\nabla f)). \quad (22)$$

From the heat equation we can then compute various fundamental operators, mainly the Laplace-Finsler operator, a generalisation of the Laplace-Beltrami operator, that describes the shape [3]. These interesting constructions are beyond the scope of this paper. For the interested reader, we point out the nice presentation and exploration of Finsler and Randers metrics and heat equation, leading to the Finsler-based Laplace-Beltrami operator [52].

B Proofs of Our Unifying Metric Theory

B.1 Proof of Theorem 3.1

Unlike most of the community, we are rephrasing the preexisting convolutions in the continuum. For now, we put aside modulation, which breaks the weight sharing assumption of convolution. Dilated convolutions scale by a factor s the reference support Δ^{ref} , usually uniformly in the image, to provide a dilated support Δ^{dil} : $\Delta^{dil} = s\Delta^{ref}$. Dilated convolution is thus given by

$$(f * g)(x) = \int_{\Delta^{ref}} f(x + sy)g(sy)dy. \quad (23)$$

In the non-standard case of using a different scale s_x for each pixel x , the support changes per pixel $\Delta_x^{dil} = s_x\Delta^{ref}$, and then dilated convolution is defined as

$$(f * g)(x) = \int_{\Delta^{ref}} f(x + s_x y)g(s_x y)dy. \quad (24)$$

In all cases, dilated convolutions can be rewritten as

$$(f * g)(x) = \int_{\Delta_x^{dil}} f(x + y)g(y)dy. \quad (25)$$

Shifted convolutions, also called entire deformable convolutions, simply shift the reference support Δ^{ref} by an offset δ_x shared by all cells

$$(f * g)(x) = \int_{\Delta^{ref}} f(x + y + \delta_x)g(y + \delta_x). \quad (26)$$

As such, if we denote $\Delta_x^{ent} = \delta_x + \Delta^{ref}$, we have for entire deformable convolutions

$$(f * g)(x) = \int_{\Delta_x^{ent}} f(x + y)g(y)dy. \quad (27)$$

On the other hand, deformable convolution introduces different offset vectors δ_x^y for each entry in the reference kernel support Δ^{ref} . Therefore, it is given by

$$(f * g)(x) = \int_{\Delta^{ref}} f(x + y + \delta_x^y)g(y + \delta_x^y)dy. \quad (28)$$

If we now write the deformed support $\Delta_x^{def} = \{y + \delta_x^y; \forall y \in \Delta^{ref}\}$, then deformed convolution can be rewritten as

$$(f * g)(x) = \int_{\Delta_x^{def}} f(x + y)g(y)dy. \quad (29)$$

We have thus managed to express these various convolutions with the same formulation

$$(f * g)(x) = \int_{\Delta_x} f(x + y)g(y)dy, \quad (30)$$

where Δ_x is either Δ^{ref} in the standard case, Δ_x^{dil} in the dilated case, Δ_x^{ent} in the entire deformable case, and Δ_x^{def} in the deformable case. If we now break the weight sharing assumption of any of

these convolutions by introducing modulation, we have mask numbers $m_x(y) \in [0, 1]$ that multiply the kernel values $g(y)$. As such, the convolutions become

$$(f * g)(x) = \int_{\Delta_x} f(x+y)g(y)m_x(y)dy. \quad (31)$$

We can then define the distribution $dm_x(y) = m_x(y)dy$ to prove the theorem and show that all these convolutions perform weighted filtering on some neighbourhood Δ_x sampled with distribution dm_x . \square

B.2 Proof of Theorem 3.2

This result is well-known. It is a direct consequence of the positive homogeneity of the metric. Assume that the UTB $B_1^t(x)$ is given at any point x . Let $u \in T_x X$ be a non zero tangent vector. Then there exists a unique $v \in B_1^t(x)$ that is positively aligned with u , i.e. there exists $\lambda > 0$ for which $v = \lambda u$, that has unit metric $F_x(v) = 1$. Note that v is the intersection of the ray with direction u (with origin x) with the boundary of $B_1^t(x)$. We can then define $F_x(u) = \lambda$. We also define $F_x(0) = 0$. We can then easily check that F_x satisfies the positive homogeneity. Given any $\lambda' > 0$, we have $\lambda' u = \lambda' \lambda v$. By construction of F_x , we thus have $F_x(\lambda' u) = \lambda' \lambda = \lambda' F_x(u)$. As easily, we can check that F_x satisfies the triangular inequality and separability. As such, the provided UTBs implicitly defines a metric F_x . \square

B.3 Reconstructing a Metric from Unit Geodesic Balls

Reconstructing the metric, or an approximation, is possible if further assumptions are introduced. For instance, if we are provided with the knowledge of distances within the unit ball, i.e. level sets within $B_1^g(x)$, or if the unit ball is sufficiently localised, i.e. $B_1^g(x)$ is sufficiently small (in Euclidean distance) to be approximated by its projection onto the tangent plane $T_x X$, then we can (approximately) reconstruct the unit tangent ball at point x and from there use Theorem 3.2 to recover the entire metric.

The issue for reconstructing metrics from UGBs is that geodesic distances consist in an integration of the metric along the tangents of the geodesics. By performing this summation, we can lose local information on the original metric. As an extreme counter-example, consider a small sphere, with radius smaller than $\frac{1}{2\pi r}$, then the unit ball at any point for the isotropic Riemannian metrics $M \equiv sI$ with $s \leq 1$ will cover the entire sphere, and likewise, other more complex metrics will provide the same unit ball. In this simplistic example, recovering the underlying metric is impossible without other prior knowledge.

B.4 Example of non-unique Metrics Explaining Discretised Sample Locations

Given a discretised sampling of a unit ball, the underlying continuous unit ball is ambiguous. As such, several metrics may provide continuous unit balls for which the given samples provide a good covering of its unit ball. We here provide two examples.

First, assume that we have finite samples and that an oracle provides us the information that these samples all lie on the unit tangent circle of some metric, i.e. $F_x(u) = 1$ for each of these samples u . Then any convex closed simple curve interpolating the provided samples yields a plausible Finsler metric F_x .

In general however, we are not aware of the distance of the sampled points within the unit ball. Sampled points do not necessarily lie at the same distance from x and no oracle provides their distance. Consider the following example. Assume we are provided with the reference template Δ^{ref} with 3×3 samples. We want to interpret it as a natural sampling of the unit tangent ball of some metric. A first natural possibility is to invoke the isotropic Riemannian Euclidean distance, for which the unit ball is the round disk³. Another possibility is to consider the traditional non-Riemannian L^∞ metric yielding unit balls in the shape of squares with straight edges parallel to those of the domain axes. Unlike the isotropic Euclidean suggestion, in the L^∞ one the samples on the border of the convex hull of the samples all lie on the unit circle of the metric.

³It would be scaled so that the radius of the unit circle is in $[\sqrt{2}, 2)$ in Euclidean measurements

Algorithm 1 Metric computation from 5 numbers

Input: Five numbers $L_{1,1}, L_{1,2}, L_{2,2}, \omega_1, \omega_2$
Hyperparameters: $\varepsilon_L > 0, \varepsilon_\omega \in (0, 1], \varepsilon > 0$
Construct $L = \begin{pmatrix} L_{1,1} & 0 \\ L_{2,1} & L_{2,2} \end{pmatrix}$ and $\omega = (\omega_1, \omega_2)^\top$
Compute $\tilde{L} = L + \varepsilon_L I$
Compute $\tilde{M} = \tilde{L}\tilde{L}^\top$
Compute $\tilde{\omega} = \frac{2(1-\varepsilon_\omega)(\sigma(\sqrt{\omega^\top M^{-1}\omega + \varepsilon}) - \frac{1}{2})}{\sqrt{\omega^\top M^{-1}\omega + \varepsilon}}\omega$
Return $(\tilde{M}, \tilde{\omega})$

C Further Discussions on the Theory of Metric Convolutions

C.1 Computing the Metric from 5 Learnt Numbers: Cholesky Approach

The most general metrics we consider in this work are Randers metrics F , which are parameterised by (M, ω) , where $M(x) \in \mathbb{R}^{2 \times 2}$ is a symmetric definite positive matrix and $\omega(x) \in \mathbb{R}^2$ must satisfy $\|\omega(x)\|_{M^{-1}(x)} < 1$. Here, we will consider a unique location x , thus for conciseness, we drop the explicit dependence on it.

This discussion explains how to compute the metric parameters γ from 5 numbers using a Cholesky-based approach. Recall the fundamental linear algebra result that symmetric definite positive matrices possess a Cholesky decomposition and vice versa.

Proposition C.1 (Cholesky decomposition). *If $M \in \mathbb{R}^{d \times d}$ is a symmetric definite positive matrix, then there exists $L \in \mathbb{R}^{d \times d}$ that is lower triangular and with only positive diagonal entries such that $M = LL^\top$.*

In our case, we can reparameterise the Riemannian metric matrix M with its Cholesky decomposition matrix L requiring only three numbers instead of 4. On the other hand, ω needs two. As such, our metric convolutions require an intermediate operation to compute 5 numbers per pixel location to fully describe the metric. By analogy with deformable convolution, we chose to use a standard convolution with only 5 output channels. Nevertheless, several issues remain. First, we need to make sure that M does not become singular. This can happen through uncontrolled optimisation if for instance the lower right entry $L_{2,2}$ becomes close to 0. Secondly, we need to enforce the norm constraint on ω for the metric to remain positive. To overcome these challenges, we used the following strategy.

To avoid the non singularity of M , we construct $\tilde{L} = L + \varepsilon_L I$, where I is the identity matrix and $\varepsilon_L > 0$ is a small number controlling the maximum scale of the metric⁴. The Riemannian component is then given by $M = \tilde{L}\tilde{L}^\top$. In our experiments, we chose $\varepsilon_L = 0.01$.

To enforce the positivity of the metric, we introduce another hyperparameter $\varepsilon_\omega \in (0, 1]$ and devise a strategy to enforce $\|\omega\|_{M^{-1}} \leq 1 - \varepsilon_\omega$. This choice would guarantee that the metric does not accumulate around 0 as then $F_x(u) \geq \varepsilon_\omega \|u\|_2$ for any tangent vector u following Proposition A.1. Taking $\varepsilon_\omega \rightarrow 1^-$ forces metric symmetry, whereas $\varepsilon_\omega \rightarrow 0^+$ allows the strongest asymmetry. Note that $\varepsilon_\omega = 1$ is equivalent to taking $\omega \equiv 0$. The strategy is the following. Compute $\|\omega\|_{M^{-1}} \in [0, \infty)$, and feed it to a modified sigmoid function to get a new number in $[0, 1 - \varepsilon_L)$. Recall that the sigmoid is defined as $\sigma(x) = \frac{1}{1+e^{-x}}$. Our modified sigmoid is thus $\tilde{\sigma}(x) = 2(1 - \varepsilon_\omega)(\sigma(x) - \frac{1}{2})$. The computed number $\tilde{\sigma}(\|\omega\|_{M^{-1}}) \in [0, 1 - \varepsilon_\omega)$ represents the desired M^{-1} -norm of the Randers drift component. As such, we could take $\tilde{\omega} = \frac{\tilde{\sigma}(\|\omega\|_{M^{-1}})}{\|\omega\|_{M^{-1}}}\omega$. An issue arises though if we are learning the metric from data and initialise with $\omega \equiv 0$, as the square root has divergent gradient at the origin. To avoid this issue, we replace the computation of $\|\omega\|_{M^{-1}}$ by the more stable $\sqrt{\omega^\top M^{-1}\omega + \varepsilon}$, where $\varepsilon > 0$ is a small number, typically $\varepsilon = 10^{-6}$, that we systematically use to avoid instabilities, e.g. divisions by 0. As such, the modified drift component forming the metric is $\tilde{\omega} = \frac{2(1-\varepsilon_\omega)(\sigma(\sqrt{\omega^\top M^{-1}\omega + \varepsilon}) - \frac{1}{2})}{\sqrt{\omega^\top M^{-1}\omega + \varepsilon}}\omega$.

We summarise the approach in Algorithm 1. Thus, when learning the metric, we use the metric defined by $(\tilde{M}, \tilde{\omega})$, and performed gradient descent on the 5 parameters of L and ω (per pixel), which is possible since \tilde{M} and $\tilde{\omega}$ are given by differentiable operations from L and ω .

⁴The smaller ε_L the larger the maximum scale, quadratically.

C.2 Computing the Metric from 6 or 7 Learnt Numbers: Spectral Approach

The previous Cholesky-based implementation (Appendix C.1) sometimes suffers from instabilities during training when combined with neural networks. This issue persisted when using an LDLT approach, where $LDL^\top = M$ and L is lower triangular with unit diagonal entries and D is positive diagonal matrix. We here present a more stable implementation to compute γ at the cost of one or two extra numbers to encode the metric.

As in Appendix C.1, we work with Randers metrics parametrised by (M, ω) and focus on a unique location x , allowing us to drop its explicit dependence on it for conciseness. Recall the fundamental linear algebra result that symmetric matrices can be diagonalised in an orthogonal basis.

Proposition C.2 (Spectral theorem). *If $M \in \mathbb{R}^{d \times d}$ is a symmetric matrix, then M can be diagonalised in an orthogonal basis. This means that there exists an orthogonal matrix $R \in \mathbb{R}^{d \times d}$ and a diagonal matrix Λ such that $M = R\Lambda R^\top$.*

As the dimensionality of the image surface manifold is $d = 2$, we could encode the rotation matrix R by an angle θ as $R = \begin{pmatrix} \cos \theta & -\sin \theta \\ \sin \theta & \cos \theta \end{pmatrix}$. Thus, only 3 numbers θ , λ_1 , and λ_2 could suffice to encode M , as in the Cholesky approach. However, regressing raw angle values is well-known to be significantly harder than estimating their cosine and sine values. This is due to periodic nature of angles: raw angle values ε and $2\pi - \varepsilon$ for small $\varepsilon > 0$ have a large difference but they correspond to almost identical angles. Instead, given two unconstrained numbers $r \in \mathbb{R}^2$, we construct the rotation matrix R using $R = \frac{1}{\|\tilde{r}\|_2 + \varepsilon} (\tilde{r} \mid \tilde{r}_\perp)$, where $\tilde{r} = r + \varepsilon$ to avoid singular R on rare instances⁵ and $\tilde{r}_\perp = (-\tilde{b}, \tilde{a})^\top$ if $\tilde{r} = (\tilde{a}, \tilde{b})^\top$.

Since M is also positive definite, then its eigenvalues $\lambda_1, \dots, \lambda_d$ forming the diagonal of Λ , are strictly positive. Given two unconstrained numbers λ_1 and λ_2 , we could construct the eigenvalue matrix $\Lambda = \begin{pmatrix} \tilde{\lambda}_1 & 0 \\ 0 & \tilde{\lambda}_2 \end{pmatrix}$, where $\tilde{\lambda}_i = |\lambda_i| + \varepsilon_L$ for $i \in \{1, 2\}$. The Riemannian component would then be given by $\tilde{M} = R\Lambda R^\top$. This strategy requires 6 numbers to compute the metric parameters γ .

However, we obtained marginally better results when separating the scale of the eigenvalues, as it introduces regularisation on them. Let s be an additional unconstrained number used to compute the scale of the eigenvalues. Denoting $\lambda'_i = 1 + 2(\sigma(\lambda_i) - \frac{1}{2}) = 2\sigma(\lambda_i) \in [0, 2]$ the ‘‘unscaled’’ eigenvalues centred around 1, we compute their scale as $\tilde{s} = \frac{s_{\min} + s_{\max}}{2} + 2(\sigma(s) - \frac{1}{2})(s_{\max} - s_{\min}) \in [s_{\min}, s_{\max}]$, where s_{\min} and s_{\max} are user-defined minimum and maximum eigenvalue scales⁶. In our experiments, we took $s_{\min} = 0.1$ and $s_{\max} = 1.5$. Finally we use the eigenvalues $\tilde{\lambda}_i = \lambda'_i \tilde{s}_i$ to build the matrix $\Lambda = \begin{pmatrix} \tilde{\lambda}_1 & 0 \\ 0 & \tilde{\lambda}_2 \end{pmatrix}$. The Riemannian component is then provided by $\tilde{M} = R\Lambda R^\top$. This strategy, requiring 7 numbers to compute the metric, is our preferred strategy and we only report results for this implementation when referring to the spectral implementation.

For both strategies, we compute the linear drift component from two unconstrained numbers ω as in Appendix C.1. This means that we use $\tilde{\omega} = \frac{\tilde{\sigma}(\|\omega\|_{M^{-1}})}{\|\omega\|_{M^{-1}}} \omega$ satisfying the norm constraints for the positivity of the metric. As we use the spectral approach for training stability, we found that we can also improve stability and marginally results by avoiding propagating the gradients through the invert operation M^{-1} . To this end, we detach the gradient of the factor $\frac{\tilde{\sigma}(\|\omega\|_{M^{-1}})}{\|\omega\|_{M^{-1}}}$ in the calculation of $\tilde{\omega}$. We used this strategy for all results reported in this work referring to the spectral implementation.

We summarise the spectral approaches using either 6 or 7 numbers in Algorithms 2 and 3. Our preferred version uses 7 numbers as it strongly encourages stability and leads to comparable or marginally better results. All results provided in this work using the spectral approach use 7 numbers. Thus, when learning the metric, we use the metric defined by $(\tilde{M}, \tilde{\omega})$, and performed gradient descent on the 7 parameters encoding the metric parameters γ (per pixel), which is possible since \tilde{M} and $\tilde{\omega}$ are given by differentiable operations from these 7 numbers.

In our experiments using a simplistic architecture – a single convolution layer for denoising (Section 5.1), we did not encounter stability issues and provide results using the Cholesky implementation for computing metric parameters γ from 5 numbers. In our experiments using complex architectures – well-established CNNs for classification (Section 5.2), we strongly benefited from

⁵We add ε here as if rigorously $r = 0$, which happened in practice on clean noiseless data like MNIST, then the vector $\frac{r}{\|r\|_2 + \varepsilon}$ would still be 0 leading to a singular matrix R .

⁶Recall that due to the inverse in Equation (3), a smaller eigenvalue scale of M leads to longer unit balls along that direction. For instance, a scale of 0.1 corresponds to stretching the ball to 10 pixels.

improved stability and provide results using only the spectral implementation for computing the metric parameters γ from 7 numbers.

Algorithm 2 Metric computation from 6 numbers

Input: Six numbers $r_1, r_2, \lambda_1, \lambda_2, \omega_1, \omega_2$
Hyperparameters: $\varepsilon_L > 0, \varepsilon_\omega \in (0, 1], \varepsilon > 0$
 Let $r = (r_1, r_2)^\top$
 Compute $\tilde{r} = r + \varepsilon$ and $\tilde{r}_\perp = (-\tilde{r}_2, \tilde{r}_1)^\top$
 Construct $R = \frac{1}{\|\tilde{r}\|_2 + \varepsilon} \begin{pmatrix} \tilde{r}_1 & \tilde{r}_{\perp,1} \\ \tilde{r}_2 & \tilde{r}_{\perp,2} \end{pmatrix}$
 Construct $\Lambda = \begin{pmatrix} |\lambda_1| & 0 \\ 0 & |\lambda_2| \end{pmatrix} + \varepsilon_L I$
 Compute $\tilde{M} = R\Lambda R^\top$
 Compute $\tilde{\omega} = \frac{2(1-\varepsilon_\omega)(\sigma(\sqrt{\omega^\top M^{-1}\omega + \varepsilon}) - \frac{1}{2})}{\sqrt{\omega^\top M^{-1}\omega + \varepsilon}} \omega$
Return $(\tilde{M}, \tilde{\omega})$

Algorithm 3 Metric computation from 7 numbers

Input: Seven numbers $r_1, r_2, \lambda_1, \lambda_2, s, \omega_1, \omega_2$
Hyperparameters: $0 < s_{\min} \leq s_{\max}, \varepsilon_\omega \in (0, 1], \varepsilon > 0$
 Let $r = (r_1, r_2)^\top$
 Compute $\tilde{r} = r + \varepsilon$ and $\tilde{r}_\perp = (-\tilde{r}_2, \tilde{r}_1)^\top$
 Construct $R = \frac{1}{\|\tilde{r}\|_2 + \varepsilon} \begin{pmatrix} \tilde{r}_1 & \tilde{r}_{\perp,1} \\ \tilde{r}_2 & \tilde{r}_{\perp,2} \end{pmatrix}$
 Compute $\lambda'_1 = 2\sigma(\lambda_1)$ and $\lambda'_2 = 2\sigma(\lambda_2)$
 Compute $\tilde{s} = \frac{s_{\min} + s_{\max}}{2} + 2(\sigma(s) - \frac{1}{2})(s_{\max} - s_{\min})$
 Compute $\tilde{\lambda}_1 = \lambda'_1 \tilde{s}$ and $\tilde{\lambda}_2 = \lambda'_2 \tilde{s}$
 Construct $\Lambda = \Lambda = \begin{pmatrix} \tilde{\lambda}_1 & 0 \\ 0 & \tilde{\lambda}_2 \end{pmatrix}$
 Compute $\tilde{M} = R\Lambda R^\top$
 Compute $\tilde{\omega} = \frac{2(1-\varepsilon_\omega)(\sigma(\sqrt{\omega^\top M^{-1}\omega + \varepsilon}) - \frac{1}{2})}{\sqrt{\omega^\top M^{-1}\omega + \varepsilon}} \omega$
Return $(\tilde{M}, \tilde{\omega})$

C.3 Polar Kernel Sampling strategies

In the continuum, the support Δ_x is given by the locations $sy_x(\theta, \gamma)$ where $s \in [0, 1]$ and $\theta \in [0, 2\pi]$. We design two complementary approaches to sample $k \times k$ grid points.

Grid sampling. To provide a $k \times k$ sampled kernel, a natural approach is to uniformly grid sample s and θ with a $k \times k$ grid.

Onion Peeling. For very small k however, e.g. $k = 3$, polar grid sampling undersamples angles, unlike standard image convolutions using a regular $k \times k$ grid. For instance, 8 angles are considered for $k = 3$ in a regular grid. To better compare with standard convolutions for small k , we propose an onion peeling sampling strategy. A standard convolution sampling $k \times k$ grid can be understood as a succession of onion layers of pixels at L^∞ distance $k' \in \{0, \dots, \lfloor \frac{k-1}{2} \rfloor\}$ from the central pixel. In the k' -th layer, there are either 1 pixel if $k' = 0$ or $8k'$ pixels for $k' \geq 1$. We use this idea to design our onion peeling metric sampling: we sample $\lfloor \frac{k-1}{2} \rfloor + 1$ values $s \in [0, 1]$ uniformly, and for each layer index $k' \in \{0, \dots, \lfloor \frac{k-1}{2} \rfloor\}$, we sample either the original point x , which is given by any θ , if $k' = 0$ or $8k'$ angles $\theta \in [0, 2\pi)$ uniformly for $k' \geq 1$.

In our denoising experiments (Section 5.1), we work with larger k , thus we used a grid sampling strategy for them. In our classification experiments using well-established CNNs (Section 5.2), these neural architectures systematically rely on 3×3 convolutions, thus we utilized an onion peeling strategy for them.

C.4 Differentiating our Metric Convolution

We focus on the continuous case from Equation (4). Differentiable changes of metric induce the variation of the unit ball in

$$\frac{\partial y_x(\theta, \gamma)}{\delta \gamma} = -\frac{1}{(F_x^\gamma)^2(u_\theta)} \frac{\partial F_x^\gamma}{\partial \gamma}(u_\theta) u_\theta. \quad (32)$$

Assuming that the convolution weights are fixed, i.e. $g(sy_x(\theta, \gamma)) = g_{\theta, s}$, differentiating the convolution with respect to the metric parameters gives

$$\frac{\partial(f * g)}{\partial \gamma}(x) = \int_{s, \theta} \left(s \frac{\partial y_x}{\partial \gamma} \right)^\top \nabla f(x + sy_x(\theta, \gamma)) g_{\theta, s} ds d\theta. \quad (33)$$

Likewise, if the metric is fixed, dependence on the weights is given by

$$\frac{\partial(f * g)}{\partial g_{\theta, s}}(x) = f(x + sy_x(\theta, \gamma)) \quad (34)$$

If needed, we can learn the parameters of the metric or the values of the kernel by gradient descent on some loss function L according to the dynamics

$$\begin{cases} \frac{\partial g_{\theta, s}}{\partial t} = -\frac{\partial L}{\partial g_{\theta, s}} \\ \frac{\partial \gamma}{\partial t} = -\frac{\partial L}{\partial \gamma}. \end{cases} \quad (35)$$

Naturally, we can generalise this to any descent-based optimisation algorithm and discrete optimisation steps.

We can easily extend this discussion to our discretised version of Equation (4).

C.5 On Difficulties for Fast Differentiable Unit Geodesic Ball Computations

In contrast to the UTB case, computing the unit geodesic balls (UGB) is expensive as it is not given by a simple closed form expression. It requires instead finding geodesic curves and then integrating along them. Many approaches exist for geodesic distance computations, and most of them require solving differential equations. They are usually either the Eikonal equation, which describes the propagation of a wave front on the manifold, or the heat equation, as initially heat diffuses along geodesics.

In the traditional Riemannian case, a wide variety of solvers exist, even differentiable ones, such as the recent differentiable fast marching algorithm [1, 2], Varadhan’s formula [51] or the idea of [13] to flow heat initially in one small time step, normalise the obtained gradient field and interpret the normalised field as the tangential components of the geodesics. Unfortunately, existing solvers are too expensive to be used in reasonable applications, such as a neural network module, and we would need to apply these solvers at least as many times as there are pixels in the image since distances are computed from the single starting points x .

An extra layer of complexity arises when using the less common Finsler metrics, for which even discretisation of differentiable operators becomes tricky. We here discuss some of these difficulties when using the idea from [13]. In Randers geometry, deriving linear solvers to length-related differentiable equations becomes highly non trivial. In the Riemannian case, this is not an issue. For instance, the Riemannian heat equation $\frac{\partial f}{\partial t} = \text{div}(\nabla f) = -\Delta_M f$ is governed by the linear Laplace-Beltrami operator Δ_M . Many works handle its possible discretisation strategies, such as the popular cotangent weight scheme [17, 39]. The linearity allows [13] to diffuse heat from a Dirac image δ_x , that are one at pixel x and zero everywhere else, by solving a set of linear equations to perform a single time-backwards iteration $(I - t\Delta_M)\delta_{x, t} = \delta_x$. The time-backwards operation essentially imagines what the heat should look like after a small time step should it have originated from the Dirac image. A forward time difference scheme would struggle to do so as the gradient of image is zero almost everywhere, and in turn the Laplace-Beltrami operator, and so almost no heat would be flown that way in a single step. This elegant solution becomes highly non trivial in the Randers case. This is why in our metric UGB convolution, we modify the approach from [13] and revert to many smaller time forward iterations to flow heat. Also, as it is unclear how to discretise operators in Randers geometry, we use a local solution rather than the global one, which provides an approximating solution satisfying some properties of the differential equation.

C.6 Details on our Naive Implementation of our metric Unit Geodesic Balls Convolutions

Finding global solutions to the Finsler heat equation (Equation (22)) is difficult. However, we can easily provide local solutions [41]. Local solutions merely satisfy some local properties of the differential equation. Our local solution, the Finsler Gauss kernel h_x [41, 55], is explicit and is given by

$$h_x(y) = \frac{1}{\mathcal{Z}(x)} \frac{1}{t} e^{-\frac{(F_x^*(y))^2}{4t}} \quad (36)$$

where F_x^* is the dual Finsler metric and is equal to the invert metric in the Riemannian case, and $\mathcal{Z}(x) = \int \frac{1}{t} e^{-\frac{(F_x^*(y))^2}{4t}} dy$ is a normalisation factor. The dual metric is beyond the scope of this paper so we refer to the Appendix A.3 for more details on it. We will just point out that the dual of a Randers metric is also a Randers metric with explicit parameters (M^*, ω^*) . We then perform a standard convolution using the Finsler Gauss kernel to diffuse the heat from a Dirac image δ_x , that are one at pixel x and zero everywhere else, to produce the diffused Dirac image $\delta_{x,t}$ according to the update rule

$$\delta_{x,t+dt}(x') = \int \delta_{x,t}(x' + y) h_{x'}(y) dy. \quad (37)$$

We can then compute the normalised gradient field $-\frac{\delta_{x,t}}{\|\delta_{x,t}\|_2}$ to get the unit speed geodesic flow field, from which we need to compute a unit ball. To get a differentiable sampling Δ_x , we can flow a stencil of points Δ^{ref} close to x given by $P_x^\gamma(s, \theta, 0) = s_0 s y_x(\theta, \gamma)$ where s_0 is an optional scaling factor and then flow for a fixed amount of time according to $\frac{\partial P}{\partial t} = -\frac{\delta_{x,t}}{\|\delta_{x,t}\|_2}$. This deforms the stencil and the obtained unit ball is no longer necessarily convex. If the initial stencil is sampled using $k \times k$ uniform polar grid points by analogy with the UTB case, the obtained stencil can be interpreted as covering the non convex unit geodesic ball (or its approximation).

This algorithm is significantly cheaper than traditional more accurate geodesic solvers, it is fully differentiable as in particular the unit ball is not obtained via a thresholding operation. However, it is still too costly to be used in real scenarii such as neural network modules. For instance, if the image has 256×256 pixels, we need to diffuse 65536 Dirac images of the same resolution and then flow 65536 sets of stencil. This either quickly occupies all available memory in RAM for single modest commercial GPUs or implies a slow sequential bottleneck for simply computing a single convolution operation.

D Experiments

D.1 Implementation Considerations of Heuristic Geometric Designs of Metric Convolutions and Other Methods and Results

We here show how to design sample locations from geometry. We take uniform kernel weights $\frac{1}{k^2}$ and no learning is involved. We denoise the 256×256 grayscale cameraman image using standard, dilated, and our metric UTB and UGB convolutions, along with deformable convolution using random offsets due to their lack of interpretability.

As mentioned in the main paper, a natural desire for the shape of unit balls when considering denoising is to be wide along the orthogonal gradient direction $\nabla f(x)^\top$ and thin along the image gradient $\nabla f(x)$. This shape avoids blurring out edges.

Unit Tangent Ball. In the UTB case, unit balls are easily given in closed form. We can thus sample them directly without having to pass through the dual metric. Our anisotropic Riemannian metric of parameter M favours the direction $\nabla f(x)^\top$ by taking it as an eigenvector with smaller eigenvalue

$$M(x) = R_{\theta_x} \begin{pmatrix} \iota \left(1 + \alpha \frac{\|\nabla f(x)\|_2}{\max\|\nabla f\|_2} \right) & 0 \\ 0 & \frac{\iota}{1 + \alpha \frac{\|\nabla f(x)\|_2}{\max\|\nabla f\|_2}} \end{pmatrix} R_{\theta_x}^\top, \quad (38)$$

where $\iota = 0.1$ controls the average metric scale⁷, $\alpha = 100$ is an anisotropy gain factor, and R_{θ_x} is the rotation matrix with angle θ_x such that $(\cos \theta_x, \sin \theta_x)^\top = \frac{\nabla f(x)}{\|\nabla f(x)\|_2 + \varepsilon}$. The small $\varepsilon = 10^{-6}$

⁷If $\nabla f(x) = 0$ then $\iota = 0.1$ creates a ball of 10 pixel edge radius.

is added here for stability and to avoid dividing by 0 in uniform areas of the image. The image gradient is computed using a Sobel filter of size 3×3 .

It is legitimate to consider symmetric neighbourhoods for denoising, i.e. $\omega \equiv 0$. Nevertheless, we also tried asymmetric metrics by controlling the scale of ω . We first compute

$$\tilde{\omega}(x) = \frac{\nabla f(x)^\top}{\|\nabla f(x)\|_2 + \varepsilon}, \quad (39)$$

and then for various scales $(1 - \varepsilon_\omega) \in \{0, 0.5, 0.9\}$, we choose

$$\omega(x) = (1 - \varepsilon_\omega) \frac{\tilde{\omega}(x)}{\|\tilde{\omega}\|_{M^{-1}(x)} + \varepsilon}. \quad (40)$$

Unit Geodesic Ball. In the UGB case, our proof of concept algorithm requires the use of the dual metric to guide the heat flow of the Dirac images. After normalising this initial flow, we reflow a stencil of points to obtain the sample locations. We use the same metric (M, ω) as in the UTB case, except that now $\alpha = 10$ and $\iota = 1$. From this metric, we can explicitly compute (M^*, ω^*) given Proposition A.2. For each pixel x , we diffuse the Dirac image δ_x , equal to 1 at pixel x and 0 everywhere, until $t = 0.1$ with time steps $dt = 0.01$. This means that starting from δ_x we iteratively convolved with the Finsler Gauss kernel 10 times.

We then define a stencil of $k \times k$ points $P(s, \theta, 0) = s_0 \text{sy}_x(\theta, (M^*, \omega^*))$ with a uniform grid of radial values $(s, \theta) \in [0, 1] \times [0, 2\pi)$ sampled $k \times k$ times. The stencil is to flow along the diffused Dirac image $\delta_{x,t}$. We diffuse for the same amount of time as the heat diffusion with the same time steps. Tuning s_0 is of interest but was not searched, we simply took $s_0 = 2$. For small s_0 , all the points in the stencil will lie in the pixel x , and when using bilinear interpolation they can decenter early from x before this drift is magnified. This behaviour is compatible with what is observed in deformable convolution. Too large values of s_0 will place stencil points in areas with unreliable normalised flow as they are at most barely reached by the heat diffusion. Flowing is done using a simple time forward scheme.

Our suggested implementation is fully differentiable but prohibitively expensive from a space and time perspective for more common application such as neural network compatibility. It merely provides a proof of concept of UGB metric convolutions.

Unit Ball Plots. To improve visualisation in Figure 3, we slightly modified the hyperparameters in the UTB and UGB case. In the UTB plots, we take $\alpha = 10$. In the UGB plots, diffusion of the Dirac image is done with time steps $dt = 0.1$ until time $t = 0.5$, whereas the stencil is flown with time steps $dt = 0.1$ until time 1.

Details of Other Methods. All convolutions used in Figure 5 use $k \times k$ samples with $k = 11$. Dilated convolution has a dilation factor of 3. Deformable convolution uses a dilation factor of 1 and each offset of each kernel cell for each pixel location is randomly, independently, and uniformly chosen in $[-\frac{k}{2}, \frac{k}{2}]^2$. Standard convolution covers a $k \times k$ pixel area and lacks interpolation, which further filters out noise, yet our method employs it. For fairness, we also test a non-standard interpolated convolution with $k \times k$ uniform samples covering a fixed smaller area. In practice, the interpolated standard convolution uses $k \times k$ uniform samples in a 5×5 pixel area. We chose this area as it is a common size of non interpolated standard convolutions. As such, the interpolated standard convolution can be seen as a standard 5×5 convolution equipped with the extra filtering from interpolation. Note that interpolated standard convolutions can also be understood as non-standard dilations with dilation factor less than 1.

Results. Results in Figure 5 show our metric convolutions outperforming standard, dilated, and deformable convolution. Metric convolutions offer interpretability to flexible convolutions and strong geometric adaptable priors beneficial for basic tasks like noise filtering. The asymmetric drift component ω degrades performance for Gaussian noise filtering but could be useful in intrinsically asymmetric tasks like motion deblurring.

D.2 Learning Filtering on a Single Image

In this experiment, we learn convolution kernel shapes for deformable and UTB convolutions with fixed uniform kernel weights using the Cholesky-based implementation. Learning is performed on a single noisy cameraman image with varying noise levels $\sigma_n \in \{0.1, 0.3, 0.5\}$ and tested on

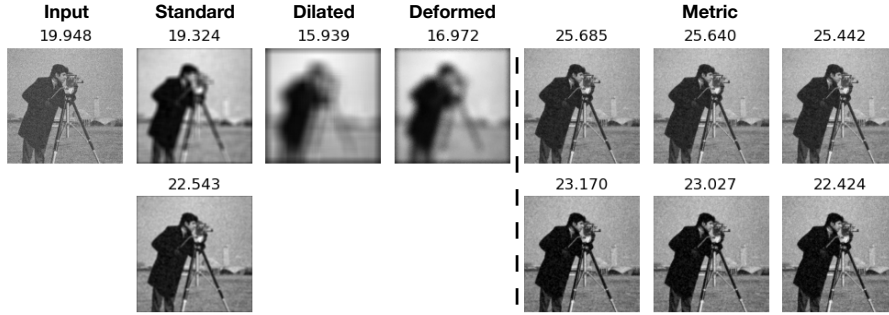


Figure 5: Denoising results using 11×11 samples from left to right: input, standard, dilated, randomly deformed, and metric convolutions with $\varepsilon_\omega = 1, 0.5, 0.1$. The bottom standard convolution uses interpolation on a smaller area. For our metric convolutions, the top row uses unit tangent balls, and the bottom row uses geodesic balls. Displayed values are the PSNR (higher is better).

Table 5: Denoising test MSE results (top) on a single noisy grayscale cameraman image when training on a different single noisy version, with noise level σ_n . Filters use $k \times k$ samples at each pixel location. Positional parameters of the convolutions are learnt, but weights are fixed. We also give the normalised generalisation gap δ_{MSE} . The parameter $\varepsilon_\omega \in (0, 1]$ controls the tolerated amount of metric asymmetry, with $\varepsilon_\omega = 1$ being symmetric. For all numbers, lower is better. Best test MSE are in bold, and second best are underlined.

		Deformable					$\varepsilon_\omega = 0.9$					Unit tangent ball (ours)					$\varepsilon_\omega = 0.1$				
		5	11	31	51	121	5	11	31	51	121	5	11	31	51	121	5	11	31	51	121
MSE	0.1	2.00E-3	4.49E-3	1.46E-2	2.24E-2	5.49E-2	<u>1.68E-3</u>	<u>1.57E-3</u>	<u>1.54E-3</u>	<u>1.54E-3</u>	<u>1.54E-3</u>	1.60E-3	1.46E-3	1.44E-3	1.42E-3	1.41E-3	1.60E-3	1.46E-3	1.44E-3	1.42E-3	1.41E-3
	0.3	7.26E-3	8.97E-3	1.99E-2	2.83E-2	6.18E-2	8.13E-3	<u>7.43E-3</u>	<u>7.58E-3</u>	<u>8.64E-3</u>	<u>8.28E-3</u>	<u>8.10E-3</u>	7.32E-3	7.45E-3	7.52E-3	7.82E-3	7.32E-3	7.45E-3	7.52E-3	7.82E-3	
	0.5	7.86E-3	1.20E-2	2.23E-2	3.07E-2	6.50E-2	1.85E-2	<u>1.68E-2</u>	1.70E-2	1.70E-2	<u>1.72E-2</u>	<u>1.84E-2</u>	1.70E-2	<u>1.73E-2</u>	<u>1.72E-2</u>	1.71E-2	1.84E-2	1.70E-2	<u>1.73E-2</u>	<u>1.72E-2</u>	1.71E-2
δ_{MSE}	0.1	5.3	3.0	1.6	1.3	0.9	0.6	0.5	0.7	0.7	0.7	0.7	0.6	0.7	0.9	1.1	0.7	0.6	0.7	0.9	1.1
	0.3	265	74	28	18	6.6	1.1	0.9	1.1	0.8	1.2	1.3	1.1	1.3	1.4	1.5	1.3	1.1	1.3	1.4	1.5
	0.5	4554	971	210	113	35	0.8	1.3	1.8	2.0	2.2	1.3	1.3	1.6	2.1	2.9	1.3	1.3	1.6	2.1	2.9

another noisy version of the same image with the same noise level. Gradient descent on the Mean Squared Error (MSE) loss is employed to optimise raw offsets and metric parameters, rather than those provided by a standard convolution as we only operate on cameraman images. This experiment evaluates if convolutions learn the image surface structure or just overfit to random noise. Convolutions use $k \times k$ samples with $k \in \{5, 11, 31, 51, 121\}$, and training runs for 100 iterations. Surprisingly, both methods require high learning rates (of magnitude 10^4 to 10^8), differing from typical rates or those in the original deformable convolution works [15, 59]. A fixed learning rate did not yield meaningful results in all setups, necessitating a search for a good learning rate each time (see Appendix D.4 for details).

Full quantitative performance is given in Table 5, where we give the MSE on the train and test image, along with the normalised generalisation gap $\delta_{MSE} = \frac{MSE_{test} - MSE_{train}}{MSE_{train}}$. We also provide full qualitative results in Appendix D.5.

D.3 Training Details for Learning Filtering on a Dataset

We trained all models using stochastic gradient descent for 100 epochs on the MSE loss with a learning rate chosen through logarithmic grid search (see Appendix D.4) that is the same for the sample locations and the kernel weights following the default methodology of [15]. Training involved various kernel sizes $k \in \{5, 11, 31\}$ on a single small commercial GPU. For $k = 31$, the batch size was reduced to 4 to fit GPU memory, and was 32 otherwise.

D.4 Learning Rate Search for Denoising Convolution Filters

The learning rate for denoising convolution filters, whether they be of deformable convolution or our metric UTB convolution, or having fixed or learnable kernel weights, were found with a learning rate finder using a logarithmic grid search on the train data for a single epoch [46]. We report in Tables 6 and 7 the chosen learning rates.

Table 6: Chosen learning rates for training the positional parameters on a single noisy image in the experiments of Table 5.

		Deformable					Unit tangent ball (ours)									
							$\varepsilon_\omega = 0.9$					$\varepsilon_\omega = 0.1$				
$\sigma_n \backslash k$		5	11	31	51	121	5	11	31	51	121	5	11	31	51	121
0.1	4.6E6	2.4E7	1.9E8	6.1E8	1.1E9	3.7E5	4.0E5	4.5E5	5.7E5	5.7E5	2.5E5	3.0E5	4.0E5	4.0E5	6.0E5	
0.3	1.5E6	7.4E6	6.0E7	1.9E8	9.8E8	1.0E4	1.0E4	1.0E4	1.2E5	1.4E5	1.0E4	1.0E4	1.0E4	1.0E4	1.1E5	
0.5	5.7E5	2.9E6	2.4E7	7.6E7	4.9E8	1.0E3	5.0E3	1.0E4	1.0E4	1.0E4	2.0E3	5.0E3	1.0E4	1.0E4	1.0E4	

Table 7: Chosen learning rates for training the positional parameters on noisy image datasets in the experiments of Table 2.

		Deformable						Unit tangent ball (ours)											
		FKW			LKW			$\varepsilon_\omega = 0.1$						$\varepsilon_\omega = 0.9$					
$\sigma_n \backslash k$		5	11	31	5	11	31	FKW			LKW			FKW			LKW		
		5	11	31	5	11	31	5	11	31	5	11	31	5	11	31	5	11	31
BSDS300	0.1	5.7E2	3.4E3	1.0E4	1.0E-2	1.0E-2	6.6E-4	6.0E0	3.1E0	7.0E-1	1.0E-2	1.0E-2	1.0E-3	6.1E0	1.1E0	1.0E0	5.0E-2	1.0E-2	1.0E-3
	0.3	3.2E2	1.5E3	1.0E4	1.0E-2	1.0E-2	6.6E-4	1.0E0	1.0E-1	1.0E-1	1.0E-1	1.0E-2	1.0E-3	1.0E0	1.1E0	1.0E-1	1.0E-2	1.0E-2	1.0E-3
	0.5	2.5E2	1.5E3	1.0E4	1.0E-2	1.0E-2	6.6E-4	6.1E-1	3.2E-1	4.5E-2	1.0E-2	1.0E-2	1.0E-3	1.0E0	3.8E-1	3.1E-2	1.0E-2	1.0E-2	1.0E-3
PASCALVOC	0.1	4.1E2	4.0E3	4.0E3	1.0E-2	1.0E-2	1.0E-3	1.2E1	4.3E0	5.0E-2	1.0E-1	1.0E-2	1.0E-3	1.4E1	1.5E0	1.0E0	1.0E-2	1.0E-2	1.0E-3
	0.3	3.0E2	4.0E3	4.0E3	1.0E-2	1.0E-2	1.0E-3	1.5E0	1.0E-1	5.0E-2	1.0E-2	1.0E-2	1.0E-3	4.0E0	5.0E-1	1.0E-1	1.0E-1	1.0E-2	1.0E-3
	0.5	4.1E2	1.1E3	4.3E3	1.0E-2	1.0E-2	1.0E-3	4.3E-1	1.0E-2	1.0E-2	1.0E-2	1.0E-2	1.0E-3	8.1E0	3.8E-1	1.0E-2	1.0E-2	5.0E-3	1.0E-3

D.5 Further Visual Results on Learning Convolutions on a Single Image

We provide in Figures 6 to 11 visual comparisons of learnt deformable and metric UTB convolutions, when learning only the shape of the convolution and keeping the filtering weights fixed. These results correspond to the quantitative ones in Table 5.

In each of these figures, two consecutive rows of plots correspond to results with a fixed noise standard deviation σ_n and number of samples $k \times k$ for the convolution. Each of these sets of two rows of plots are organised as follows. Top left is the groundtruth image and bottom left is the train and test MSE during training. Starting from the second column, the top row corresponds to train whereas the bottom one refers to test. Starting from the second column, from left to right: input noisy image, deformable convolution result, our metric UTB convolution results with different $\varepsilon_\omega \in \{0.9, 0.1\}$ controlling the scale of ω , with $\omega \equiv 0$ for $\varepsilon_\omega = 1$. Numbers provided correspond to the PSNR with respect to the groundtruth image, with higher scores being better.

Note that using an extremely high number of samples, e.g. 121×121 , does not increase the size of the sampling domain for our metric UTB convolution as the unit ball does not depend on the sample size. Larger kernels imply more samples in the same unit ball. On the other hand, deformable convolution suffers from high number of samples as it relies on the reference template of 121×121 pixels, which in our experiments is half the image size in width. As such, in many pixel locations, the reference support overlaps with the outside of the image, where it is padded to 0, which makes it impossible for gradient-descent based strategies to learn meaningful offsets in such cases.

D.6 Implementation Considerations of CNN Classification

We here use the common ResNet terminology. All traditional ResNet architectures are a succession of *layers*. The initial layer, sometimes called *conv1*, has a single convolution module, along with other operations. Following the initial layer, comes a succession of four layers, named *layer1*, *layer2*, *layer3*, *layer4*. Each of these layers consist in a sequence of convolution *blocks*. These blocks can be *basic* for smaller networks like ResNet18, or *bottleneck* ones for larger versions like ResNet50 and ResNet152. Each block of a network has the same structure, up to a final pooling. Basic blocks have two 3×3 convolution modules, whereas bottleneck blocks have only one, when no downsampling is involved. None of these convolutions have an additional bias term. The first 3×3 convolution of the first block of every layer has a stride of 2, whereas all the other have a stride of 1. All convolutions use a dilation of 1 (no dilation).

In the experiments of Tables 3 and 4, we directly replace only the 3×3 convolution modules with their 3×3 adaptive counter-parts, i.e. deformable, shifted, and our UTB convolution. We use the same number of input and output channels and no bias. Only the convolutions in layer2, layer3, and layer4 are changed. Those in layer1 or conv1 are unchanged and remain standard. We also change the stride of the first convolution of the first block of layer4 from 2 to 1 and to avoid decreasing the receptive field we increase its dilation from 1 to 2. A dilation different from 1 impacts the position of the reference kernel Δ^{ref} of deformable and shifted convolutions, and does not impact our metric convolution. The methodology described here is a direct imitation of that of

[15, 59, 56]. However, unlike [59, 56], we do not use modulation for simplicity as explained in the main paper: we wish to preserve the weight sharing assumption and sample uniformly the unit balls.

We propose to initialise our metric UTB convolution modules in the following way. Denoting c_{in} the number of input channels, kernel weights are initialised (and fixed in FKW) to $z_{k,c_{in}} = \frac{1}{c_{in}k^2}$. As for the weights of intermediate standard convolution with 5 output channels computing the metric parameters $L_{1,1}$, $L_{1,2}$, $L_{2,2}$, ω_1 , and ω_2 in this order, we initialise them as follows per output channel: the first and third ones have uniform weights set to $z_{k,c_{in}}$, and the other ones are set uniformly to $\varepsilon = 10^{-6}$. In particular, this means that $\omega \approx 0$ initially, and the network must learn how much asymmetry is best. For simplicity however, we took $\omega = 0$ always, i.e. restricting the metric to Riemannian ones, by taking $\varepsilon_\omega = 1$. We also took $\varepsilon_L = 0.01$.

Like in the previous experiments, we test both fixing the kernel weights (FKW) of the non-standard convolutions to uniform values and learning only the sample locations, or learn simultaneously sample locations and the weights (LKW). Note that FKW has never been tested in the community of non-standard convolutions for neural networks. Prior works [31] start only with pretrained weights, up to module conversion, obtained on ImageNet [16] classification with vanilla modules. We argue that such a methodology does not properly reflect the strengths of convolutions with changeable supports. Indeed, we only switch a convolution with another one, thus the obtained network is still a CNN, albeit non-standard and theoretically more general. It should thus still provide good results when weights are learned from scratch. We thus train either from scratch (SC) or do transfer learning (TL) by starting from pretrained weights obtained on ImageNet.

All networks are trained for 240 epochs with the Adam optimizer [26] on the cross-entropy loss. We take a batch size of 128, a base learning rate of $\eta = 0.0001$, and we use cosine annealing [36] for scheduling the learning rate with maximal temperature $T_{\max} = 240$ as is commonly done. Following the common practice, images fed to the networks are centred and normalised following the dataset mean and standard deviation. It takes about 7 hours to train on CIFAR a metric CNN on a single GTX 2080 Ti GPU.

For all datasets, including both train and test splits, input images are first normalised according to the training dataset’s mean and standard deviation. Since MNIST and Fashion-MNIST are curated datasets with objects centred and roughly aligned, we do not need data augmentation to train the models. However, the natural images in CIFAR-10 and CIFAR-100 are not, and therefore we apply data augmentation on training images by randomly cropping the input image to a patch, resizing the patch to the full image size, and then randomly horizontally flipping the image.

All CNNs with our metric UTB convolutions use the onion peeling sampling polar kernel sampling strategy (Appendix C.3) and the metric computation from 7 numbers (Algorithm 3), except for those with fixed kernel weights (FKW) which use the version with 6 numbers (Algorithm 2). On CIFAR-10 and CIFAR-100, we got marginally better results when training the networks with learnable kernel weights (LKW) using an L1 regularisation loss on the weights of the intermediate convolutions with a Lagrangian coefficient of 5000. On CIFAR-10 with learnable weights and transfer-learned (LKW-TL), we got even slightly better results when using 50 warmup epochs, where during the warmup the output of the intermediate convolution is multiplied by 0. This warmup imitates the baseline sampling strategy of a fixed kernel while still using our metric framework.

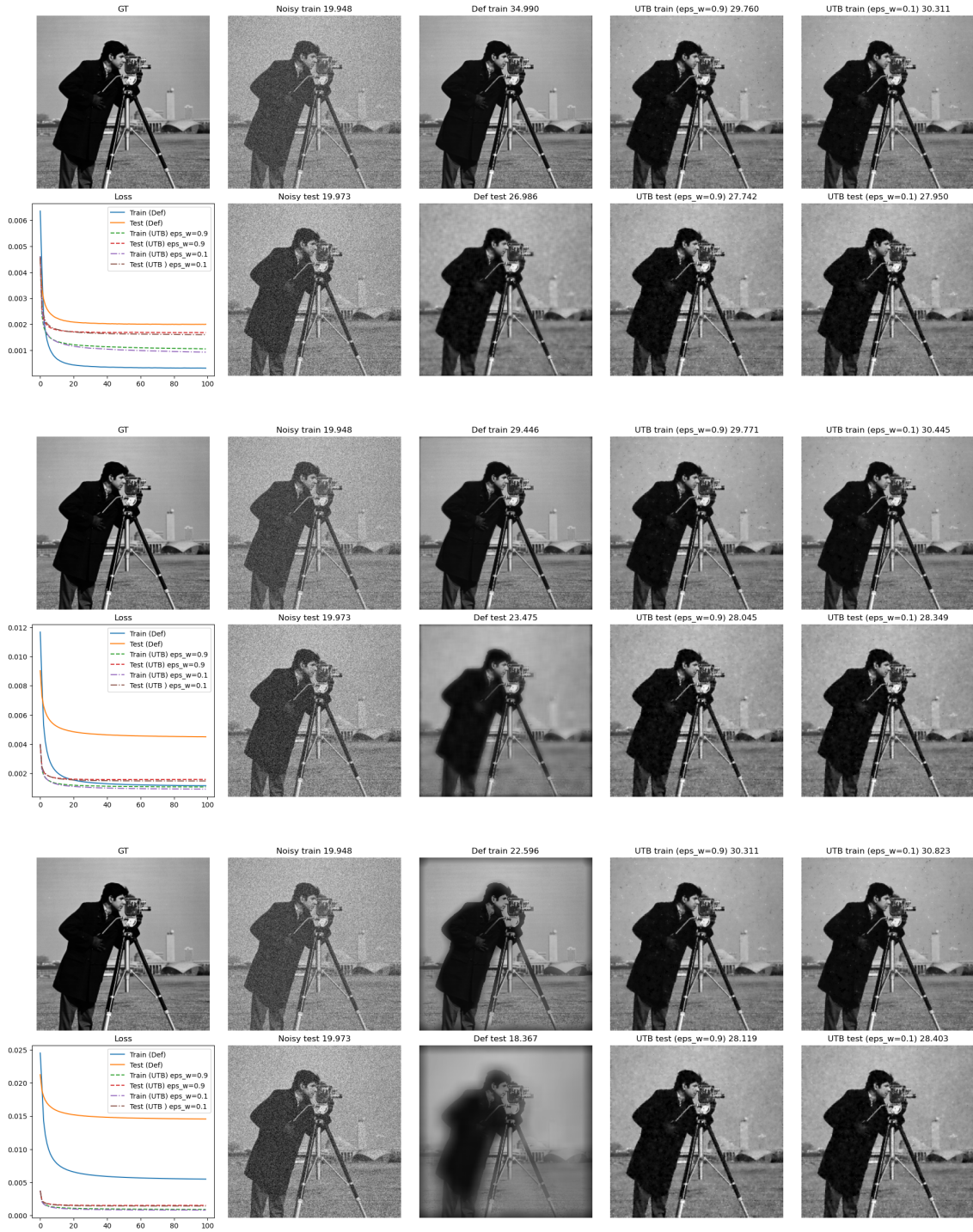


Figure 6: Results of learnt deformable and our metric UTB convolutions with $\sigma_n = 0.1$ and $k = 5, 11, 31$, from top to bottom.



Figure 7: Results of learnt deformable and our metric UTB convolutions with $\sigma_n = 0.1$ and $k = 51, 121$ from top to bottom.

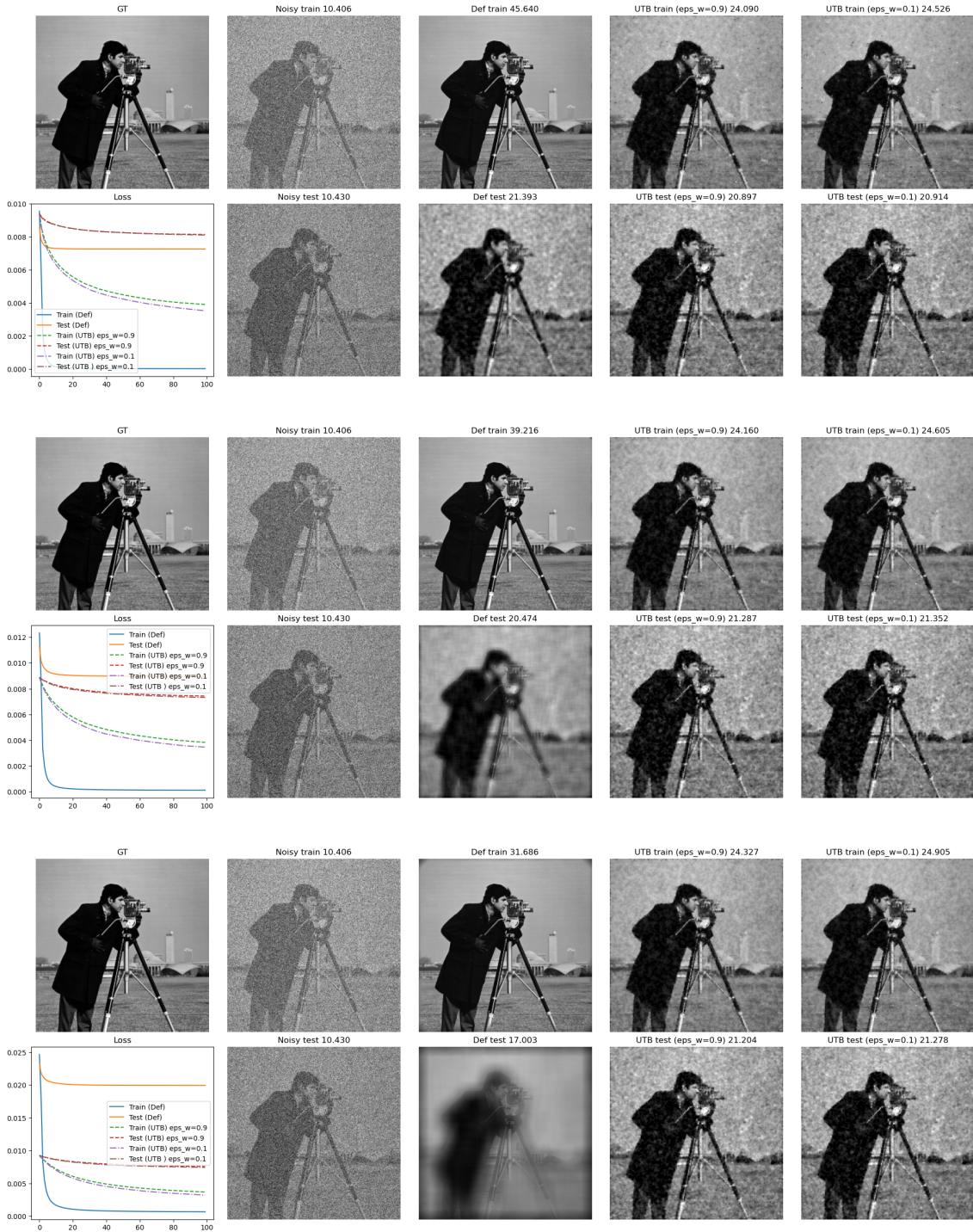


Figure 8: Results of learnt deformable and our metric UTB convolutions with $\sigma_n = 0.3$ and $k = 5, 11, 31$ from top to bottom.



Figure 9: Results of learnt deformable and our metric UTB convolutions with $\sigma_n = 0.3$ and $k = 51, 121$ from top to bottom.

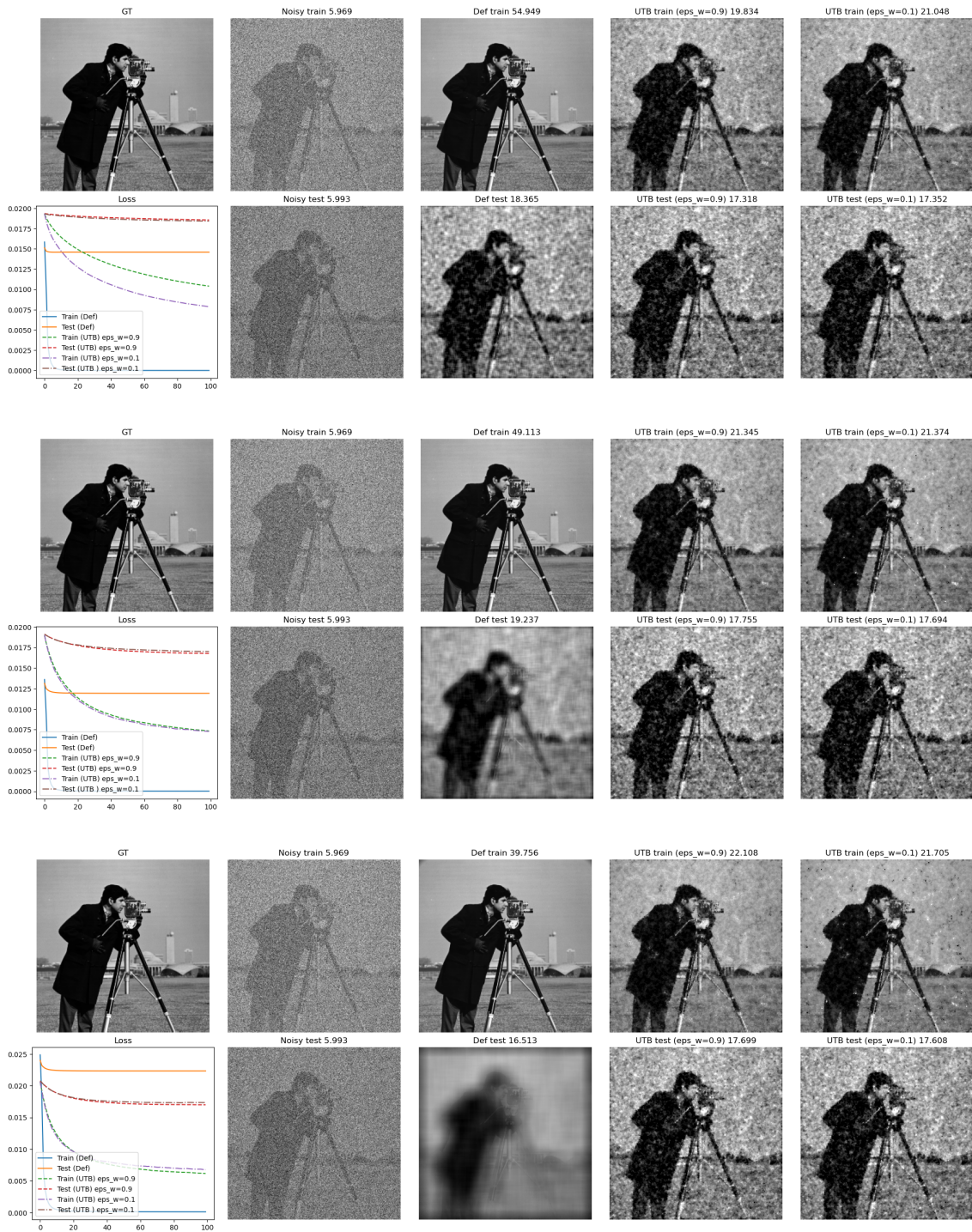


Figure 10: Results of learnt deformable and our metric UTB convolutions with $\sigma_n = 0.5$ and $k = 5, 11, 31$ from top to bottom.

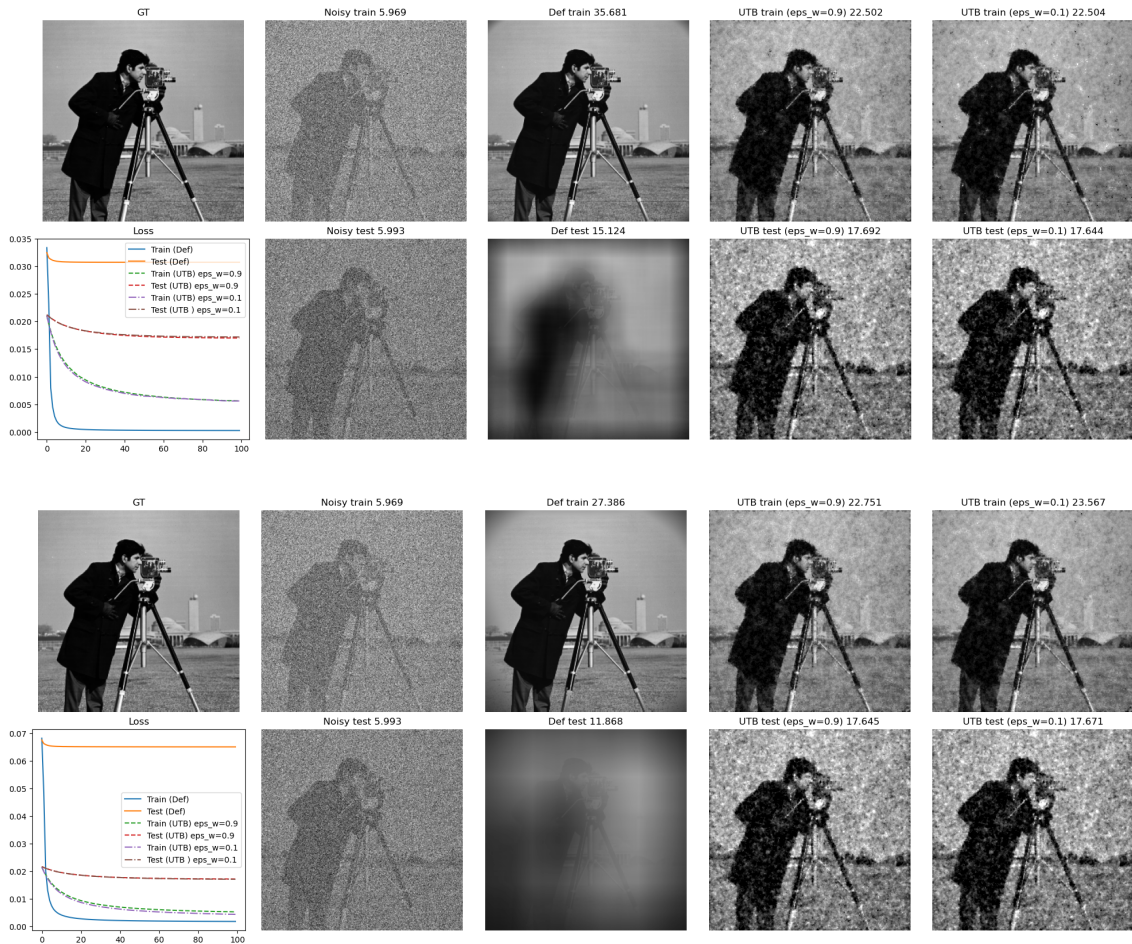


Figure 11: Results of learnt deformable and our metric UTB convolutions with $\sigma_n = 0.5$ and $k = 5, 11, 31$ from top to bottom.